



The Mass Accretion Rate and Stellar Properties in Class I Protostars

Eleonora Fiorellino^{1,2,3} , Łukasz Tychoniec⁴ , Fernando Cruz-Sáenz de Miera^{1,2} , Simone Antonucci⁵ ,
Ágnes Kóspál^{1,2,6,7} , Carlo F. Manara⁴ , Brunella Nisini⁵ , and Giovanni Rosotti^{8,9,10}

¹ Konkoly Observatory, Research Centre for Astronomy and Earth Sciences, Eötvös Loránd Research Network (ELKH), Konkoly-Thege Miklós út 15-17, 1121 Budapest, Hungary; eleonora.fiorellino@inaf.it

² CSFK, MTA Centre of Excellence, Budapest, Konkoly Thege Miklós út 15-17., H-1121, Hungary

³ INAF-Osservatorio Astronomico di Capodimonte, via Moirariello 16, I-80131 Napoli, Italy

⁴ European Southern Observatory, Karl-Schwarzschild-Strasse 2, D-85748 Garching bei München, Germany

⁵ INAF-Osservatorio Astronomico di Roma, via di Frascati 33, I-00078, Monte Porzio Catone, Italy

⁶ Max Planck Institute for Astronomy, Königstuhl 17, D-69117 Heidelberg, Germany

⁷ ELTE Eötvös Loránd University, Institute of Physics, Pázmány Péter sétány 1/A, 1117 Budapest, Hungary

⁸ Leiden Observatory, Leiden University, PO Box 9513, NL-2300 RA Leiden, The Netherlands

⁹ School of Physics and Astronomy, University of Leicester, University Road, Leicester LE1 7RH, UK

¹⁰ Dipartimento di Fisica “Aldo Pontremoli,” Università degli Studi di Milano, via G. Celoria 16, I-20133 Milano, Italy

Received 2022 July 30; revised 2022 October 27; accepted 2022 November 12; published 2023 February 17

Abstract

Stars collect most of their mass during the protostellar stage, yet the accretion luminosity and stellar parameters, which are needed to compute the mass accretion rate, are poorly constrained for the youngest sources. The aim of this work is to fill this gap, computing the stellar properties and the accretion rates for a large sample of Class I protostars located in nearby (<500 pc) star-forming regions and analyzing their interplay. We used a self-consistent method to provide accretion and stellar parameters by modeling the spectral energy distribution and using veiling information from near-IR observations when possible. We calculated accretion and stellar properties for the first time for 50 young stars. We focused our analysis on the 39 confirmed protostars, finding that their mass accretion rate varies between $\sim 10^{-8}$ and $\sim 10^{-4} M_{\odot} \text{ yr}^{-1}$ in a stellar mass range between ~ 0.1 and $3 M_{\odot}$. We find systematically larger mass accretion rates for our Class I sample than for Class II objects. Although the mass accretion rate we found is high, it still suggests that either stars collect most of their mass before the Class I stage, or eruptive accretion is needed during the overall protostellar phase. Indeed, our results suggest that for a large number of protostars the disk can be unstable, which can result in accretion bursts and disk fragmentation in the past or in the future.

Unified Astronomy Thesaurus concepts: Star formation (1569); Stellar accretion disks (1579); Stellar properties (1624); Protostars (1302); Low mass stars (2050); Circumstellar disks (235); Circumstellar dust (236)

1. Introduction

Young stars acquire mass by accreting material from the infalling envelope and the circumstellar disk. In particular, according to the magnetospheric accretion scenario (Hartmann et al. 2016), the accretion flow proceeds from the disk to the forming star along the magnetic field lines. The accretion rate is supposed to be very large during the protostellar phase (Class 0 and I), where the accretion luminosity (L_{acc}) is larger than the stellar luminosity (L_{\star}), then it decreases with time in the pre-main-sequence (PMS) phase (Class II), until accretion basically stops (Class III).

In this context, the mass accretion rate (\dot{M}_{acc}) is a fundamental parameter in the star formation process, because it links the properties of the forming star with the evolution of the protoplanetary disk. This parameter is well constrained in classical T Tauri (or Class II) young stellar objects (YSOs), for which the \dot{M}_{acc} can be directly measured from the ultraviolet (UV) excess over the stellar photosphere caused by the accretion shock (e.g., Calvet & Gullbring 1998; Gullbring et al. 1998; Herczeg & Hillenbrand 2008; Rigliaco et al. 2012;

Ingleby et al. 2013; Fairlamb et al. 2015; Rugel et al. 2018; Schneider et al. 2020).

In recent years, many surveys of \dot{M}_{acc} in classical T Tauri stars (CTTS) have been provided (see Manara et al. 2022, for a review). These have been carried out using the UV excess and/or the empirical correlations between the accretion luminosity (L_{acc}) and the luminosity of accretion tracers, such as the Balmer, Paschen, and Brackett lines (e.g., Muzerolle et al. 1998; Alcalá et al. 2017). In contrast, \dot{M}_{acc} for the earlier stages is known only for a few sources (Muzerolle et al. 1998; Nisini et al. 2005; Antonucci et al. 2008; Yen et al. 2017), despite the fact that most of the accretion onto the forming star occurs during the protostellar phase. The reason behind this is the difficulty of computing accretion rate in such embedded objects. Large extinction and veiling of those young protostars prevent us from studying the UV and optical emission, forcing the analysis to be carried out using infrared (IR) wavelengths. At those longer wavelengths the contributions of the disk, photosphere, outflows and jets, and envelope are entangled and complicated to analyze separately.

Recent efforts to characterize stellar properties of the youngest stars (e.g., Fiorellino et al. 2021; Laos et al. 2021) as well as available archival observations (Muzerolle et al. 1998; White & Hillenbrand 2004; Doppmann et al. 2005; Connelley & Greene 2010) show a promising way to investigate the protostellar phase. We continue this effort,

aiming to study the accretion process during such an early stage of the star formation, by providing results for 39 protostars, enlarging our accretion survey of Class I protostars by a factor of three. In this work we will discuss the question: what can we infer about the protostellar accretion process from the current state of the art?

2. Sample

This work is based on the already existing observations of low-mass protostellar sources within 500 pc published in the literature. We divide the sample into three subsamples based on how the stellar parameters and the mass accretion rates have been computed.

The first subsample consists of 50 protostars for which we calculated stellar parameters and accretion rates for the first time in this work using archival observations (Section 2.1); another subsample of 18 protostars is a collection of YSOs with published accretion rates and stellar parameters already present in the literature and directly comparable with the analysis performed in this work (Section 2.2); lastly, a subsample of 27 protostars is collected from the literature, consisting of sources analyzed with indirect methods whose results are not directly comparable with other samples, but which we add for comparison (Section 2.3).

In order to study stellar properties together with protoplanetary disk masses, for all the subsamples we searched for archival data to collect millimeter fluxes, from which we calculate the disk dust mass (M_{dust}).

2.1. Mass Accretion Rate and Stellar Parameters Computed in This Work

The first sample is taken from the NASA Infrared Telescope Facility (IRTF) *K*-band spectroscopic survey of 110 young stars by Connelley & Greene (2010, CG10). The sources for this survey have been selected from the all-sky IRAS catalog; they were classified as Class I sources by Lada (1991) and collected in Connelley et al. (2008).

CG10 provided veiling information for 50 out of 110 objects, based on either continuum fitting or photospheric absorption. For the remaining 60 sources, the veiling was too high and a reliable estimate could not be provided. Since veiling is a fundamental parameter in our analysis we narrow down the sample to 50 sources with the veiling measurement available.

Thus we note that in the analysis we are limited toward sources with low veiling value. The maximum veiling value is about ~ 8 . Since, by definition, large veiling means larger accretion flow, considering only low-veiled young stars implies a bias toward less accreting Class I YSOs.

In Table 1 we summarize 50 sources from CG10 with their measured properties. In CG10 the source evolution class has been assigned based on the classification of Lada (1991). We have updated it, considering sources with $-0.3 < \alpha < 0.3$ as flat-spectrum sources (“Flat” sources, Greene et al. 1994), in order to highlight the sources in transition between evolutionary Classes I and II; however, in further analysis we consider Flat sources and Class I as protostellar sources and we refer to all of them as Class I objects.

Additionally, it has more recently been suggested that several objects are more evolved than indicated by their spectral index, based on different protostellar properties

(Guieu et al. 2006; Furlan et al. 2008, 2016; Howard et al. 2013; Sadavoy et al. 2019). In particular, four of them (namely, IDs 08, 12, 14, and 35) are Class II young stars (see Appendix A), therefore we discarded them from our sample. Six sources (namely, IDs 04, 19, 32, 37, 41, and 43) are eruptive sources classified as FU Ori objects, or FUors (see Appendix B). Standard methods of obtaining stellar and accretion properties are not reliable for FUors, and therefore we consider them separately.

This results in a final sample of 40 Class I protostars; we were able to estimate the stellar and accretion parameters for only 39 of them (Section 3).

2.2. Mass Accretion Rate and Stellar Parameters from the Literature: Direct Measurements

In addition to the sample from CG10, we have compiled archival information on Class I sources from the literature for which the accretion rates and stellar parameters were computed using a similar methodology to that we adopted in this work (see Section 3.3), based on near-IR accretion tracers. This includes 18 Class I YSOs from Nisini et al. (2005), Antonucci et al. (2008), and Fiorellino et al. (2021). Nisini et al. (2005) computed the accretion luminosity by subtracting the stellar luminosity from the bolometric luminosity and showing that this value is in agreement with empirical relations linking H I emission lines and L_{acc} by Muzerolle et al. (1998). Antonucci et al. (2008) used this result to build up the same self-consistent method we use in this work (see Section 3.3) by assuming 1 Myr as the age of their protostars. Fiorellino et al. (2021) updated the same aforementioned self-consistent method by using the most recent empirical relations by Alcalá et al. (2017) and assuming the age of these sources to be between the birthline (BL, Palla & Stahler 1990) and 1 Myr old, considering the Spitzer-based lifetimes (Enoch et al. 2009; Dunham et al. 2014). Table 2 shows the list of these protostars together with their stellar and accretion properties, which are directly comparable with results of the sample described in the previous section.

2.3. Mass Accretion Rate and Stellar Parameters from the Literature: Indirect Measurements

Obtaining direct measurements of stellar properties for the youngest sources is challenging; however, there exist a number of indirect methods to derive stellar and accretion parameters that we describe below. In Table 3, we collect information on bolometric luminosity, stellar mass, and disk dust mass of protostars (9 Class 0 and 12 Class I sources in addition to our 39 + 18 Class I protostars).

M_{\star} has been provided by inferring the mass of a central object responsible for the Keplerian rotation of the circumstellar disk (e.g., Lommen et al. 2008; Lee 2010; Chou et al. 2014), except for source WL 16 (Miotello et al. 2014) where M_{\star} is obtained from L_{bol} with standard assumptions on \dot{M}_{acc} and placing a star on the birthline. We also note that if the estimate depends on the distance (e.g., bolometric luminosity and disk dust mass), we scaled it to the current best estimate for the distance (see Section 3.1).

It should be noted that other stellar properties such as stellar and accretion luminosity and mass accretion rate can be obtained for some protostars using indirect methods and with assumptions on stellar evolutionary track. Compilations of

Table 1
Sources Selected from the CG10 Sample

ID	IRAS Name	Simbad Name	α	Class	R.A. Decl. (J2000)	$W_{\text{eq}}^{\text{Br}\gamma}$ (Å)	r_K	m_K (mag)	L_{bol} (L_{\odot})	SpT	T_{eff} (K)
1 ^b	03220+3035	[CG2010] IRAS 03220+3035(N)	0.02	Flat	03:25:09.43 30:46:21.6	-1.71 ± 0.29	$0.0^{+0.88}_{-0.0}$	10.57 ± 0.05	...	M2	3490
2	03301+3111	2MASS J03331284+3121241	0.31	I	03:33:12.84 31:21:24.1	-2.31 ± 0.08	$0.48^{+0.84}_{-0.3}$	10.58 ± 0.05	4.0	M2	3490
3	03507+3801	IRAS 03507+3801	0.22	Flat	03:54:06.19 38:10:42.5	-0.64 ± 0.57	$0.6^{+2.16}_{-0.36}$	9.91 ± 0.06	2.5	G7	5290
4 ^F	04108+2803	NAMEIRAS 04108+2803A	-0.15	II (1)	04:13:53.39 28:11:23.4	-1.72 ± 0.41	$0.24^{+1.20}_{-0.24}$	10.37 ± 0.02	...	M2	3490
5	04113+2758	[BHS98] MHO1	-0.13	Flat	04:14:26.27 28:06:03.3	-3.22 ± 0.16	$0.60^{+1.94}_{-0.0}$	8.20 ± 0.05	1.1	M2	3490
6 ^b	04113+2758	[BHS98] MHO2	-0.13	Flat	04:14:26.40 28:05:59.7	-1.45 ± 0.20	$0.00^{+0.72}_{-0.00}$	8.27 ± 0.05	1.1	M2	3490
7	04169+2702	IRAS 04169+2702	0.53	I	04:19:58.45 27:09:57.1	-1.50 ± 0.09	$0.60^{+1.20}_{-0.24}$	11.26 ± 0.06	0.9	M2	3490
8 ^b	04181+2655	[MDM2001] CFHT-BD-Tau19	1.96	II (2)	04:21:07.95 27:02:20.4	-0.89 ± 0.06	$0.12^{+3.84}_{-0.12}$	10.54 ± 0.06	...	G7	5290
9	04181+2655	NAMEIRAS 04181+2654B	...	I	04:21:10.39 27:01:37.3	-8.41 ± 0.14	$0.00^{+1.44}_{-0.00}$	10.34 ± 0.06	...	G7	5290
10 ^b	04189+2650	V*FS Tau	...	I	04:22:02.18 26:57:30.5	-1.74 ± 0.06	$0.72^{+1.20}_{-0.00}$	8.28 ± 0.06	40.0	M2	3490
11	04189+2650	2MASS J04220069+2657324	-0.04	Flat	04:22:00.70 26:57:32.5	-6.48 ± 0.21	$4.9^{+2.8}_{-2.8}$	12.03 ± 0.07
12	04240+2559	V*DG Tau	-0.26	II	04:27:04.70 26:06:16.3	-7.78 ± 0.07	$0.00^{+1.68}_{-0.00}$	6.78 ± 0.05	3.5	G3	5740
13	04248+2612	IRAS 04248+2612	0.52	I	04:27:57.30 26:19:18.4	-2.75 ± 0.25	$0.00^{+2.76}_{-0.00}$	10.62 ± 0.05	0.3	M3	3360
14	04292+2422	Haro 6-13	0.01	II (3)	04:32:15.41 24:28:59.7	-2.62 ± 0.11	$0.12^{+2.52}_{-0.00}$	7.63 ± 0.05	0.6	G7	5290
15	04295+2251	IRAS 04295+2251	0.13	Flat	04:32:32.05 22:57:26.7	-1.10 ± 0.08	$0.54^{+1.08}_{-0.30}$	10.54 ± 0.07	0.3	M2	3490
16	04315+3617	IRAS 04315+3617	-0.05	Flat	04:34:53.22 36:23:29.2	-10.22 ± 0.43	$3.6^{+2.6}_{-2.1}$	9.20 ± 0.05	1.7
17 ^b	04381+2540	IRAS 04381+2540	0.64	I	04:41:12.68 25:46:35.4	-2.30 ± 0.18	$0.24^{+0.66}_{-0.24}$	11.81 ± 0.05	0.6	K5	4140
18	04530+5126	V*V347 Aur	0.05	Flat	04:56:57.02 51:30:50.9	-2.47 ± 0.10	$0.36^{+1.32}_{-0.00}$	7.80 ± 0.06	...	M2	3490
19 ^F	04591-0856	IRAS 04591-0856	0.62	I	05:01:29.64-08:52:16.9	-1.41 ± 0.21	$0.18^{+0.06}_{-0.18}$	10.40 ± 0.07	0.9	K7	3970
20	05289-0430	IRAS 05289-0430	0.38	I	05:31:27.09-04:27:59.4	-2.85 ± 0.08	$8.0^{+5.0}_{-3.5}$	9.61 ± 0.05	7.1
21	05311-0631	2MASS J05333251-0629441	0.23	Flat	05:33:32.52-06:29:44.2	-2.79 ± 0.10	$1.32^{+1.32}_{-0.48}$	10.14 ± 0.07	7.3	M4	3160
22	05357-0650	Paranago 2649	0.01	Flat	05:38:09.31-06:49:16.6	-0.72 ± 0.04	$5.32^{+0.00}_{-3.78}$	7.93 ± 0.03	10.8	A0	...
23 ^b	05375-0040	Haro 5-90	0.62	I	05:40:06.79-00:38:38.1	-2.59 ± 0.07	$0.00^{+1.96}_{-0.00}$	8.51 ± 0.02	7.1	G7	5290
24 ^b	05375-0040	2MASS J05400637-0038370	...	I	05:40:06.37-00:38:37.0	-1.61 ± 0.08	$0.42^{+0.70}_{-0.28}$	10.28 ± 0.03	...	M2	3490
25 ^b	05375-0040	2MASS J05400579-0038429	...	I	05:40:05.79-00:38:43.0	-5.77 ± 0.07	$0.14^{+1.26}_{-0.14}$	9.46 ± 0.02	...	G7	5290
26	05379-0758	2MASS J05402054-0756398	...	I	05:40:20.55-07:56:39.9	-6.10 ± 0.10	$5.0^{+2.0}_{-5.0}$	9.35 ± 0.03	6.4
27	05379-0758	[MB91] 54	0.19	Flat	05:40:20.31-07:56:24.9	-2.35 ± 0.19	$0.12^{+1.02}_{-0.12}$	10.86 ± 0.03	...	K2	4760
28 ^{bAL}	05384-0808	2MASS J05405059-0805487	1.03	Flat (4)	05:40:50.59-08:05:48.7	-1.80 ± 0.14	$0.30^{+1.02}_{-0.30}$	11.48 ± 0.04	10.8	M2	3490
29	05384-0808	2MASS J05404991-0806084	...	Flat (4)	05:40:49.92-08:06:08.4	-2.73 ± 0.15	$0.54^{+1.50}_{-0.06}$	11.15 ± 0.04	...	M2	3490
30	05405-0117	IRAS 05405-0117	0.71	Flat (4)	05:43:03.06-01:16:29.2	-3.06 ± 0.20	$1.56^{+1.08}_{-1.56}$	10.25 ± 0.05	4.4	M2	3490
31	05427-0116	IRAS 05427-0116	0.63	I	05:45:17.31-01:15:27.6	-0.26 ± 0.28	$0.36^{+1.08}_{-0.24}$	10.92 ± 0.05	2.5	M2	3490
32 ^E	05513-1024	V*V1818 Ori	0.18	Flat	05:53:42.55-10:24:00.7	-2.02 ± 0.10	$8.8^{+4.8}_{-3.2}$	5.96 ± 0.02	...	F0	7280
33 ^b	05555-1405	2MASS J05574946-1405278	0.62	I	05:57:49.46-14:05:27.8	-8.14 ± 0.13	$4.9^{+4.4}_{-4.9}$	10.62 ± 0.05	4.8
34	05555-1405	2MASS J05574918-1406080	...	I	05:57:49.18-14:06:08.0	-1.09 ± 0.08	$0.54^{+1.14}_{-0.48}$	10.86 ± 0.05	...	M2	3490
35	16240-2430	WL 16	0.24	II (5)	16:27:02.34-24:37:27.2	-8.09 ± 0.08	$0.8^{+0.4}_{-0.8}$	7.82 ± 0.06	...	A0	...
36 ^b	16288-2450	[CG2010] IRAS 16288-2450(W1)	0.70	I	16:31:52.98-24:56:24.6	-2.71 ± 0.18	$1.20^{+1.08}_{-1.08}$	7.85 ± 0.05	...	M2	3490
37 ^F	16289-4449	V346 Nor	-0.04	Flat	16:32:32.19-44:55:30.7	-2.26 ± 0.11	$6.3^{+4.0}_{-4.3}$	7.21 ± 0.08	5.9
38	16316-1540	JCMTSP J163429.4-154700	0.84	I	16:34:29.29-15:47:01.9	-0.64 ± 0.07	$0.00^{+1.32}_{-0.00}$	8.28 ± 0.05	11.4	K0	5030
39	16442-0930	2MASS J16465826-0935197	0.22	Flat	16:46:58.27-09:35:19.7	-2.99 ± 0.34	$1.4^{+1.4}_{-1.2}$	10.92 ± 0.03	0.7
40	18275+0040	IRAS 18275+0040	-0.19	Flat	18:30:06.17 00:42:33.6	-1.83 ± 0.08	$11.2^{+25.0}_{-5.0}$	7.72 ± 0.06	3.4
41 ^F	18341-0113	2MASS J18364633-0110294	0.91	I	18:36:46.33-01:10:29.5	-1.66 ± 0.55	$0.12^{+2.16}_{-0.00}$	9.80 ± 0.05	...	M2	3490
42 ^b	18577-3701	V*S CrA	0.12	Flat	19:01:08.61-36:57:20.1	-6.50 ± 0.07	$4.8^{+0.5}_{-2.9}$	6.11 ± 0.05	1.5

Table 1
(Continued)

ID	IRAS Name	Simbad Name	α	Class	R.A. Decl. (J2000)	$W_{\text{Br}\gamma}^{\text{Br}\gamma}$ (Å)	r_K	m_K (mag)	L_{bol} (L_{\odot})	SpT	T_{eff} (K)
43 ^F	19266+0932	Parsamian 21	0.37	I	19:29:00.86 09:38:42.9	-0.18 ± 0.28	$0.00_{-0.00}^{+2.28}$	9.68 ± 0.07	3.4	3	5740
44	20355+6343	LDN 1100	0.59	I	20:36:22.86 63:53:40.4	-1.65 ± 0.10	$3.9_{-3.9}^{+30}$	10.40 ± 0.05	2.5
45	21445+5712	IRAS 21445+5712	0.54	I	21:46:07.12 57:26:31.8	-0.63 ± 0.12	$5.1_{-3.3}^{+2.6}$	10.25 ± 0.13	18.5
46	22266+6845	IRAS 22266+6845	0.53	I	22:28:02.99 69:01:16.7	-1.82 ± 0.08	$0.12_{-0.12}^{+1.56}$	10.49 ± 0.05	1.8	K2	4760
47	22272+6358	IRAS 22272+6358B	1.76	I	22:28:57.60 64:13:37.5	-2.42 ± 0.09	$0.0_{-0.0}^{+4.44}$	8.18 ± 0.05	15.5	F3	6660
48	22324+4024	EM*LkHA 233	0.08	Flat	22:34:41.01 40:40:04.5	-2.19 ± 0.06	$8.4_{-1.3}^{+2.2}$	9.46 ± 0.10	11.6	F3	6660
49	23037+6213	2MASS J23054976+6230011	1.23	I	23:05:49.76 62:30:01.2	-2.90 ± 0.09	$0.60_{-0.12}^{+4.44}$	9.04 ± 0.10	30.2	F3	6660
50	23591+4748	2MASS J00014325+4805189	0.60	I	00:01:43.25 48:05:19.0	-2.81 ± 0.19	$0.84_{-0.84}^{+1.32}$	10.42 ± 0.05	...	M2	3490

Note. Effective temperature (T_{eff}) from Pecaut & Mamajek (2013) for the spectral type (SpT). Additional properties: **binarity**, **FUor**, or **EXor** object (Connelley & Greene 2010). **bAL** = ALMA binary. Class: evolutionary class of the object, classified according to its IR spectral index (Lada 1991; Greene et al. 1994). In cases where the classification has been found to be likely different according to other indicators, a reference is provided: (1) Furlan et al. (2008), (2) Guieu et al. (2006), (3) Howard et al. (2013), (4) Furlan et al. (2016), (5) Sadavoy et al. (2019). The bolometric luminosity L_{bol} , SpT, and T_{eff} are only shown for comparison with our results in Tables 4 and 5.

Table 2
Class I Previously Known from the Literature Analyzed with the Same or a Similar Method to That Used for This Work

ID	Name	Distance (pc)	L_{bol} (L_{\odot})	r_K	A_V (mag)	L_{acc} (L_{\odot})	L_{\star} (L_{\odot})	T_{eff} (K)	M_{\star} (M_{\odot})	R_{\star} (R_{\odot})	Age (yr)	\dot{M}_{acc} ($M_{\odot} \text{ yr}^{-1}$)	M_{dust} (M_{\oplus})	References
1	IRS2	160	12	7.7 ± 2.5	4.3 ± 1.5	4900 ± 200	1.4 ± 0.3	2.9 ± 0.5	0.5–1	3×10^{-7}	694 ± 2	(a)
2	IRS5a	160	2	0.4	1.6 ± 0.5	4200 ± 200	0.5 ± 0.1	1.0 ± 0.1	0.3–0.5	3×10^{-8}	587 ± 2	(a)
3	IRS6a	160	0.3	<0.1	0.5 ± 0.2	3580 ± 100	0.3 ± 0.1	0.1 ± 0.1	0.5–1	$<5 \times 10^{-9}$...	(a)
4	HH 100 IR	160	14	12 ± 2	3.1 ± 0.9	4060 ± 300	0.4 ± 0.1	6.0 ± 0.5	0.1	2×10^{-6}	444 ± 8	(a)
5	IRS3	160	0.3	<0.1	0.3 ± 0.1	3800 ± 100	0.5 ± 0.1	0.2 ± 0.1	1–5	$<9.6 \times 10^{-9}$...	(a)
6	HH 26 IRS	450	4.6 – 9.2	...	4.1	3.2	3.7	K7	0.6	8.5×10^{-7}	469 ± 18	(b)
7	HH 34 IRS	460	12.4 – 19.9	...	4.9	13.3	2.9	M0	0.5	41.1×10^{-7}	2283 ± 68	(b)
8	HH 46 IRS	450	<15.0	...	4.9	1.5	6.0	K5	1.2	2.2×10^{-7}	1127 ± 15	(b)
9	J03283968 +31117321 ^a	293 ± 22	0.31	3–8	43.0 – 51.0	0.04 – 0.10	0.25 – 0.31	2818–3038	0.13 – 0.20	1.6 – 2.2	BL–1 Myr	$(1.4\text{--}8.3) \times 10^{-8}$	12.8 ± 0.8	(c)
10	J03285842 +3122175 ^a	293 ± 22	1.11	3–8	31.0 – 34.5	0.57 – 0.86	0.25 – 0.54	3020–3218	0.11 – 0.25	1.8 – 2.5	BL–1 Myr	$(19\text{--}70) \times 10^{-8}$	11.3 ± 0.6	(c)
11	J03290149 +3120208 ^a	293 ± 22	18.2	3–8	45.0 – 52.0	2.46 – 5.70	12.5 – 15.7	4942–5248	2.80 – 3.03	4.5 – 4.9	BL–1 Myr	$(16\text{--}38) \times 10^{-8}$	7.7 ± 2.2	(c)
12	SVS 13 (V512 Per) ^b	293 ± 22	58.8	3–8	33.0–39.0	16.4–33.7	25.1–42.5	5173–5754	3.07–3.53	2.1–5.7	BL–1 Myr	$(19\text{--}220) \times 10^{-8}$	969.7 ± 15.5	(c)
13	LAL96 213	293 ± 22	7.63	3–8	17.0–41.0	1.72–4.01	3.62–5.91	3802–4683	0.70–1.90	3.1–4.7	BL–1 Myr	$(13\text{--}120) \times 10^{-8}$	318.5 ± 0.9	(c)
14	J03290895 +3122562 ^a	293 ± 22	0.23	1–3	15.5–22.5	0.02–0.04	0.19–0.22	2754–3002	0.11–0.15	1.4–2.1	BL–1 Myr	$(0.7\text{--}3.3) \times 10^{-8}$...	(c)
15	J03290907 +3121291 ^a	293 ± 22	0.51	3–8	36.5–41.0	0.20–0.34	0.17–0.31	2754–3075	0.11–0.20	1.4–2.1	BL–1 Myr	$(7\text{--}28) \times 10^{-8}$	–	(c)
16	J03291188 +3121271 ^a	293 ± 22	0.12	1–3	19.0–25.5	0.01–0.03	0.09–0.11	2754–2928	0.10–0.11	1.0–2.1	BL–1 Myr	$(0.6\text{--}2.6) \times 10^{-8}$...	(c)
17	J03292003 +3124076 ^a	293 ± 22	0.59	1–3	26.0–34.0	0.03–0.07	0.52–0.56	3020–3289	0.19–0.28	2.1–2.5	BL–1 Myr	$(0.8\text{--}3.6) \times 10^{-8}$	3.8 ± 1.6	(c)
18	J03292044 +3118342 ^a	293 ± 22	0.70	1–3	12.5–20.0	0.06–0.15	0.55–0.64	3020–3289	0.19–0.28	2.2–2.5	BL–1 Myr	$(2.0\text{--}8.1) \times 10^{-8}$...	(c)

Notes.

^a Two Micron All Sky Survey name of the sources (the prefix 2MASS has been removed). (a) Nisini et al. (2005); (b) Antonucci et al. (2008); (c) Fiorellino et al. (2021).

^b Binary system.

Table 3

Class 0 and I Protostars Collected from the Literature with Stellar and Accretion Properties Obtained with Alternative Methods to Those in Table 2 and in This Work

ID	Name	Notes	Class	D (pc)	L_{bol} (L_{\odot})	M_{\star} (M_{\odot})	M_{dust} (M_{\oplus})
1	B335	...	0 ¹	106 ± 15 ²	0.8 ¹	0.05 ³	14 ± 4 ⁴
2	IRAS 16253-2429	...	0 ⁵	144 ± 9 ⁶	0.09 ⁵	0.03 ± 0.01 ⁷	9.2 ± 1.2 ⁸
3	VLA 1623A	...	0 ¹	144 ± 9 ⁶	4.8 ^{1,*}	0.22 ± 0.02 ⁹	129 ± 16 ¹⁰
4	IRAS 15389-3559	...	0 ¹¹	155 ± 4 ¹²	1.5 ¹¹	0.007 ± 0.004 ¹³	5.8 ± 0.3 ¹³
5	Lupus 3-MMS	...	0 ¹⁴	162 ± 3 ¹⁵	0.27 ^{14,*}	0.3 ± 0.1 ⁷	213 ± 8 ⁷
6	L1455 IRS1	b ¹⁶	0 ¹⁷	293 ± 22 ¹⁸	4.94 ¹⁷	0.32 ³	175 ± 16 ¹⁹
7	IRAS 4A2	...	0 ¹	293 ± 22 ¹⁸	<14.1 ^{1,*} ,+	0.08 ± 0.02 ²⁰	1637 ± 148 ¹⁹
8	L1157	b ²¹	0 ¹	352 ± 19 ⁶	7.9 ^{1,*}	0.04 ²²	985 ± 195 ²³
9	HH 212	...	0 ²⁴	400 ± 40 ²⁵	13.5 ²⁴	0.3 ± 0.1 ²⁶	474 ± 95 ²⁵
10	L1527	...	I ¹	141 ± 9 ⁶	2.5 ¹	0.19 ± 0.04 ²⁷	221 ± 28 ²⁸
11	L1551-IRS5	b ²⁹	I ¹	141 ± 9 ⁶	22.9 ^{1,*}	0.2 ± 0.1 ³⁰	526 ± 83 ³¹
12	TMC 1A	...	I ¹	141 ± 9 ⁶	2.6 ¹	0.56 ³²	210 ± 34 ³³
13	L1489 IRS	...	I ³⁴	141 ± 9 ⁶	3.5 ³⁴	1.64 ± 0.12 ³⁵	52 ± 8 ³⁵
14	L1551-NE	b ³⁶	I ³⁷	141 ± 9 ⁶	4.2 ³⁷	0.8 ³⁸	187 ± 24 ³⁹
15	WL 12	...	I ¹	144 ± 9 ⁶	1.9 ^{1,*}	3.8 ^{40,*}	62 ± 8 ⁴¹
16	Elias 29	...	I ¹	144 ± 9 ⁶	19.3 ^{1,*}	3.2 ± 0.6 ⁴²	15.6 ± 2.0 ⁴³
17	IRS 63	...	I ³⁴	144 ± 9 ⁶	2.0 ^{34,*}	0.8 ⁴⁴	305 ± 38 ⁴⁵
18	IRS 43	b ⁴⁶	I ¹⁴	144 ± 9 ⁶	1.4 ^{14,*}	1.9 ⁴⁴	15 ± 2 ⁴³
19	RCrA IRS 7B	b ⁴¹	I ¹	155 ± 4 ¹²	6.5 ^{1,*}	2.3 ⁴⁷	393 ± 17 ⁴¹
20	HH 111	b ⁴⁸	I ³⁷	411 ± 41 ²⁵	23 ³⁷	1.3 ⁴⁹	187 ± 24
21	EC 53	...	I ¹⁷	436 ± 9 ⁵⁰	5.4 ¹⁷	0.3 ± 0.1 ⁵¹	381 ± 16 ⁵¹

Note. *: scaled for updated distance; +: upper limit, property derived from unresolved observation; b: binary system, the mass of the disk and stellar mass is from the sum of the two components. ¹Karska et al. (2018), ²Olofsson & Olofsson (2009), ³Yen et al. (2015), ⁴Bjerkeli et al. (2019), ⁵Dunham et al. (2008), ⁶Zucker et al. (2019), ⁷Yen et al. (2017), ⁸Hsieh et al. (2019a), ⁹Murillo & Lai (2013), ¹⁰Sadavoy et al. (2018), ¹¹Yang et al. (2018), ¹²Galli et al. (2020), ¹³Okoda et al. (2018), ¹⁴Dunham et al. (2013), ¹⁵Dzib et al. (2018), ¹⁶Tobin et al. (2016a), ¹⁷Dunham et al. (2015), ¹⁸Ortiz-León et al. (2018), ¹⁹Tobin et al. (2018), ²⁰Choi et al. (2010), ²¹Tobin et al. (2022), ²²Kwon et al. (2015), ²³Chiang et al. (2012), ²⁴Furlan et al. (2016), ²⁵Tobin et al. (2020), ²⁶Codella et al. (2014), ²⁷Tobin et al. (2012), ²⁸Nakatani et al. (2020), ²⁹Looney et al. (1997), ³⁰Chou et al. (2014), ³¹Cruz-Sáenz de Miera et al. (2019), ³²Aso et al. (2015), ³³Harsono et al. (2021), ³⁴Green et al. (2013), ³⁵Sai et al. (2020), ³⁶Reipurth et al. (2002), ³⁷Froebich (2005), ³⁸Takakuwa et al. (2013), ³⁹Takakuwa et al. (2017), ⁴⁰estimated from L_{bol} , assuming M_{acc} and birthline (Miotello et al. 2014), ⁴¹ALMA: 2019.1.01792.S, ⁴²Lommen et al. (2008), ⁴³Sadavoy et al. (2019), ⁴⁴Brinch & Jørgensen (2013), ⁴⁵Segura-Cox et al. (2020), ⁴⁶Girart et al. (2000), ⁴⁷Lindberg et al. (2014), ⁴⁸Reipurth et al. (1999), ⁴⁹Lee (2010), ⁵⁰Ortiz-León et al. (2017), ⁵¹Lee et al. (2020).

some of those properties for protostars are presented in Yen et al. (2017) and Sai et al. (2020), where then-known rotationally supported disks are listed and their host star properties are summarized.

We acknowledge that those properties may be less reliable than in direct measurements described in Sections 2.1 and 2.2. However, this addition not only offers insight into the sources where direct measurements are very challenging (e.g., very extinguished sources as Class 0 and high-veiled Class I protostars), but also sheds some light on the reliability of these indirect methods. Examples of the other indirect methods to derive stellar properties are briefly summarized below.

Doppmann et al. (2005) measured L_{\star} from H - and K -band photometry corrected for extinction with the caveat that the accretion could contribute to these fluxes. Prato et al. (2009) obtained L_{acc} from $\text{Br}\gamma$ flux measurements, K -band photometry, and spectral typing by comparing with standard stars. Lee (2010) estimated L_{\star} using the assumption $R_{\star} = 3 R_{\odot}$ and M_{\star} from the Keplerian rotation of the gas in the disk, assuming that the accretion rate onto the star is equal to the infall rate onto the disk. In Miotello et al. (2014), the effective temperature (T_{eff}) is derived from L_{bol} by placing a star on the birthline from Palla & Stahler (1990). Sheehan & Eisner (2018) obtained stellar luminosity through radiative transfer modeling of the spectral energy distribution (SED). From this, a stellar radius can be obtained, and then M_{\star} is provided by following assumption $\dot{M}_{\text{acc}} = 10^{-5} M_{\odot} \text{ yr}^{-1}$. Alternatively, M_{\star} can be provided by inferring the mass of a central object responsible for the Keplerian rotation of the circumstellar disk

(Lommen et al. 2008; Lee 2010; Chou et al. 2014). The mass accretion rate can be approximated from L_{bol} where R_{\star} is assumed to be $3 R_{\odot}$ and M_{\star} is derived from Keplerian rotation of the disk (Yen et al. 2017).

3. Analysis

In this section, we describe how we computed the distance, the bolometric luminosity (L_{bol}), and the disk mass (M_{disk}) for the overall sample. We also discuss the computation of the accretion rates and stellar parameters for the sample in Table 1. The accretion rates and stellar parameters for sources in Tables 2 and 3 have already been computed in the literature.

3.1. The Distance

We verified the distances to our targets with the most recent estimates. If available, direct measurement of the parallax from Gaia EDR3 was used to update the distance (Gaia Collaboration et al. 2021). In many cases the sources in our sample are too deeply embedded to be measured with Gaia and therefore we adopted the distance of the parent cloud obtained with Gaia (Akeson et al. 2019; Yan et al. 2019; Tobin et al. 2020; Krolikowski et al. 2021) or other methods (Wouterloot & Brand 1989; Hilton & Lahulla 1995; Anglada & Rodríguez 2002; Kóspál et al. 2008; Ortiz-León et al. 2018). Additionally, for source 2MASS J05574918-1406080 (ID 34) a large discrepancy was found between parallax and photogeometric method (Bailer-Jones et al. 2020), and since the latter has a smaller uncertainty and is more consistent with distance

to the other sources nearby, we chose this method instead of the parallax measurement.

3.2. The Bolometric Luminosity

The bolometric luminosity is a critical parameter in our analysis. Calculation of L_{bol} relies on good sampling of the SED of the protostellar sources. We used the SEDBYS v.2.0 Python-based package (Davies 2021) to extract photometry and build SEDs (figures in Appendix C). In addition to the catalogs available in the SEDBYS package, we cross-checked our list of targets with catalogs of dense cores: Herschel (Marsh et al. 2016; Pezzuto et al. 2021), Herschel PACS Point Source Catalog (European Space Agency 2017a), Herschel SPIRE Point Source Catalog (European Space Agency 2017b), and photometry catalog of disks in Taurus (Andrews et al. 2013). Using all the available photometry, it was possible to compute L_{bol} for every source in the sample, and to provide more accurate estimates than what is available in the literature. Absence of photometry at any specific wavelengths means that either the source was not covered by the observations or it was not detected. We did not include subarcsecond observations of the disks in the SED data because they would usually resolve out the envelope, underestimating the contribution of the envelope at those wavelengths.

We computed L_{bol} by integrating the SEDs with a dedicated Python procedure, following the method already used in the literature (Antoniucci et al. 2008; Fiorellino et al. 2021). The integration was performed starting from the shortest wavelength, and using linear interpolation in the $\log \lambda - \log(\lambda F_\lambda)$ plane between the available SED points. We also applied a final correction at the longest wavelengths ($\lambda > 100 \mu\text{m}$), assuming that the emission decreases as $1/\lambda^2$ after the last available observation. Since the available photometry differs from source to source, we adopted the following methodologies to provide homogeneous estimate of the bolometric luminosity. For sources for which photometry up to 2 mm was observed (36%), we just integrated the fluxes, as described above. For sources for which we collected photometry at $\lambda > 100 \mu\text{m}$ but no flux at 2 mm, we fit a straight line (in log-log) from the peak of the SED to the longest available wavelength to extrapolate the photometry at 2 mm, and then we proceed with the integration (44%). Lastly, several sources had no photometry at wavelengths longer than $100 \mu\text{m}$ in our data set (20%). In some cases, this is due to the fact that the source is too faint at such long wavelengths, and it is not detected. But in other cases, we are not certain whether the source has a strong emission or not at $\lambda > 100 \mu\text{m}$ since no observations at these wavelengths were performed. In these cases we integrated all the available photometry, being aware that it is possible that our results are lower limits. In the following, we highlight these sources in the relevant plots.

The derived values are shown in Table 5 and they range from $\sim 10^{-3}$ to $\sim 10^3 L_\odot$. Uncertainties on L_{bol} were computed by adopting Monte Carlo simulations.

We compared our results with the bolometric luminosity computed by CG10. They provided results for only 34 sources among our sample by using the formula discussed in Connelley et al. (2007, Equation (2)), based on the IRAS fluxes (from 12 to $100 \mu\text{m}$), and on the distance of the source, assuming the same SED model we adopt for $\lambda > 100 \mu\text{m}$. Figure 1 shows the results of this comparison: 15 sources (44%) have L_{bol} values in agreement within 3σ by using the two methods; for only three

sources is our L_{bol} estimate lower than those by CG10. We used different and updated distances than CG10, and we considered not only IRAS fluxes, but also more accurate and recent flux estimates at both shorter (e.g., Gaia 500 nm) and longer (e.g., SCUBA $850 \mu\text{m}$) wavelengths. The different methodologies should be an indicator to not expect the same values. However, we cannot neglect the trend we see in Figure 1 where our L_{bol} values are systematically larger than those provided by CG10. A possible interpretation of this trend is that by integrating over a larger wavelength range we include a larger portion of the emitted luminosity. In contrast, when our L_{bol} estimates are lower, it is possible that these sources are affected by the overestimation already pointed out by CG10. Moreover, the method adopted by CG10 infers the submillimeter flux by fitting the same 36 K blackbody to the IRAS flux at $100 \mu\text{m}$, while our analysis directly integrates observed fluxes, relying on a similar model only when data at $\lambda > 100 \mu\text{m}$ are not available. Looking at the SEDs in Appendix C, we note that all the objects for which we computed smaller L_{bol} estimates show particularly low fluxes for $\lambda > 100 \mu\text{m}$, which constrains the integral of the SEDs empirically, not considering any model.

In general, we are confident that our estimates of the bolometric luminosity are more robust because (i) we used the most updated distances based on Gaia data, (ii) we integrated for a larger wavelength range, and (iii) our SEDs are carefully and more densely sampled. All these improvements contribute to providing more accurate results.

3.3. Accretion Rates and Stellar Parameters

Measuring the mass accretion rate in embedded protostars is challenging for two main reasons. First, Class I objects are not visible in the UV, where the Balmer jump directly traces the accretion luminosity. Second, the envelope contribution of Class I sources is entangled with the disk and photosphere contributions, preventing us from computing the visual extinction (A_V), veiling, and stellar parameters with the standard methodology used for CTTS such as spectral shape fitting and analysis of absorption features. For these reasons, we adopted a self-consistent method already used in the literature to analyze Class I protostars (Antoniucci et al. 2008; Fiorellino et al. 2021).

This procedure is based on the following assumptions: (i) the bolometric luminosity is the sum of the stellar and accretion luminosities, $L_{\text{bol}} = L_\star + L_{\text{acc}}$, where the disk luminosity (L_{disk}) is reprocessed during the accretion, thus L_{disk} is “included” in the L_{acc} contribution; (ii) envelope and disk contributions, which cannot be disentangled in Class I sources, can be described by the veiling (r_K), therefore the absolute bolometric magnitude in the K band is $M_{\text{bol}} = \text{BC}_K + m_K + 2.5 \log(1 + r_K) - A_K - 5 \log(d/10\text{pc})$; (iii) the empirical relations between the luminosity of H I lines and the accretion luminosity found for CTTS are a good approximation for Class I stars (Nisini et al. 2005; Fiorellino et al. 2021), in particular the one regarding the $\text{Br}\gamma$ line, $\log L_{\text{acc}} = a \log L_{\text{Br}\gamma} + b$, where $a = 1.19 \pm 0.10$ and $b = 4.02 \pm 0.51$ (Alcalá et al. 2017). Consequently, if we know the observed K -band magnitude (m_K), $L_{\text{Br}\gamma}$, L_{bol} , the distance, and the K -band veiling (r_K), and assume the age of the object that sets the spectral type and thus the bolometric correction (BC_K), then the only free parameter is the extinction (A_K), which consistently provides the same L_\star from the computations in points (i) and (ii). For a detailed

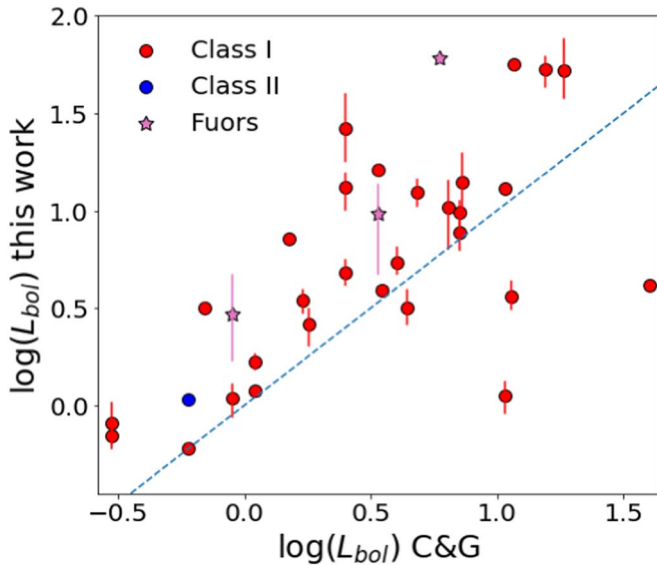


Figure 1. Comparison between the bolometric luminosity computed in this work and those computed by CG10. FUors are included in this plot (pink stars). Classes I and II are shown by red and blue circles, respectively. Uncertainties smaller than the symbol size are not plotted. The solid line indicates one-to-one correspondence.

description of this method, we refer the reader to Section 5.1 of Fiorellino et al. (2021).

To use this self-consistent method, we measured the flux of the $\text{Br}\gamma$ line ($F_{\text{Br}\gamma}$) as follows. From the K -band magnitude listed in Table 1, we computed the continuum flux that we used to convert the equivalent width of the $\text{Br}\gamma$ line (W_{eq}) into flux. Errors were computed by propagating the uncertainties provided by Connelley & Greene (2010), see Table 5. Then, the line luminosity is $L_{\text{Br}\gamma} = 4\pi d^2 F_{\text{Br}\gamma}$. We used L_{bol} computed as described in Section 3.2, and the veiling from CG10. We assumed that our sources are located between the birthline (as defined by Palla & Stahler 1993) and the 1 Myr isochrone of the Siess et al. (2000) models. Using the self-consistent method described above, we obtained both the stellar and the accretion luminosity for each protostar.

We determined the stellar mass and radius (M_* , R_*) using both the birthline and the 1 Myr isochrone from Siess et al. (2000), and the mass accretion rate using the relation

$$\dot{M}_{\text{acc}} \sim \left(1 - \frac{R_*}{R_{\text{in}}}\right)^{-1} \frac{L_{\text{acc}} R_*}{GM_*}, \quad (1)$$

where R_{in} is the inner-disk radius, which we assume to be $R_{\text{in}} \sim 5R_*$ (Hartmann et al. 1998), and G is the gravitational constant. The average errors on the accretion luminosity, stellar radius, and mass are 0.4, 0.6, and 0.1 dex, which result in a cumulative error for the mass accretion rate of 0.8 dex (Fiorellino et al. 2021). To these uncertainties we should also add the uncertainty due to the source’s variability, which is estimated to be about 0.5 mag in flux (Lorenzetti et al. 2013), propagating a variation on the flux of about 50%. The accretion luminosity, the mass accretion rate, and the stellar parameters of our sample ranging from the birthline to 1 Myr of age are listed in Table 5.

Figure 2 shows histograms of the ratios L_{acc}/L_* (top panel) and \dot{M}_{acc}/M_* (bottom panel) of our Class I sample (red line if we assume sources on the birthline, pink line if we assume the

age of the sources is 1 Myr) compared to the Lupus Class II sample (black line, Manara et al. 2022). We chose Class II objects in this cloud because they are representative of Class II PMS stars and well studied in the recent past (Alcalá et al. 2014, 2017).

The histogram of our Class I sample peaks at higher values ($\log(L_{\text{acc}}/L_*) \sim -0.9$ and $\log(\dot{M}_{\text{acc}}/M_* \text{ yr}^{-1}) \sim -6.5$) compared to Class II sample ($\log(L_{\text{acc}}/L_*) \sim -2.2$ and $\log(\dot{M}_{\text{acc}}/M_* \text{ yr}^{-1}) \sim -9.0$) for both L_{acc}/L_* and \dot{M}_{acc}/M_* . This suggests that the accretion is more intense in Class I objects than during the Class II stage. We performed a two-sample Kolmogorov–Smirnov test (KS test) on the Class I and Lupus Class II populations for both the L_{acc}/L_* and \dot{M}_{acc}/M_* distributions. We obtained probabilities of 0.32 for Class I on the birthline and 0.35 for Class I 1 Myr old for the luminosity. This means that the probability for the Class I and the Class II L_{acc}/L_* values to be drawn from the same statistical distribution is about 1/3: $0.32 < p < 0.35$. The same analysis on the \dot{M}_{acc}/M_* distributions results in probabilities of 0.10 for the Class I on the birthline and 0.15 for the Class I 1 Myr old. In other words, the probability for the Class I and the Class II \dot{M}_{acc}/M_* values to be drawn from the same statistical distribution is particularly low: $0.10 < p < 0.15$. While the L_{acc}/L_* distributions largely overlap each other (more than half of the Class I histograms are inside the Class II one), only the tail-ends of the \dot{M}_{acc}/M_* distribution overlap. This difference corresponds to the different KS test results, showing that the L_{acc}/L_* distribution in Classes I and II is more similar than the \dot{M}_{acc}/M_* distribution. This can be explained by the presence of the stellar parameters in Equation (1), in particular the radius, which is larger for younger sources in the evolutionary models we used. Also, it is important to keep in mind that while the Class II sample is a complete sample from Lupus, the Class I sample is not complete, being composed only of the brightest sources from different star-forming regions (SFRs). Thus, any intrinsic differences between the SFRs can blur the differences between classes by widening the FWHM of either histogram. This means that we mostly analyze the left side of the full histogram for all the Class I YSOs. In turn, because the p -value in the KS test uses the mean of the distributions, it is possible to speculate that we obtain lower probabilities than when also considering the most embedded Class I YSOs. More data of a complete sample belonging to a single SFR are needed to draw firm conclusions. However, the fact that we can already see differences in the \dot{M}_{acc}/M_* histograms with our incomplete and biased sample indicates that the differences will probably be much more pronounced once the Class I sample is complete.

It is also worth noting that only for eight Class I on the birthline and seven Class I on the 1 Myr evolutionary track is the accretion luminosity larger than the stellar luminosity ($L_{\text{acc}}/L_* > 1$); see the dotted–dashed cyan vertical line in Figure 2. This could also be due to an observational bias, since we are studying the less embedded Class I young stars.

To investigate which is the dominant component of the luminosity of our protostars, we plot in Figure 3 the accretion fraction as a function of the bolometric luminosity (red and blue lines represent low-veiling sources, i.e., $r_K < 3$, and high-veiling sources, i.e., $r_K > 3$, respectively), and we compare this sample with the NGC 1333 protostars from Fiorellino et al. (2021) (pink and black lines represent low-veiled and high-veiled sources, respectively). Most of the sources in their main accretion phase (i.e., $L_{\text{acc}}/L_{\text{bol}} > 0.5$) have a high veiling value

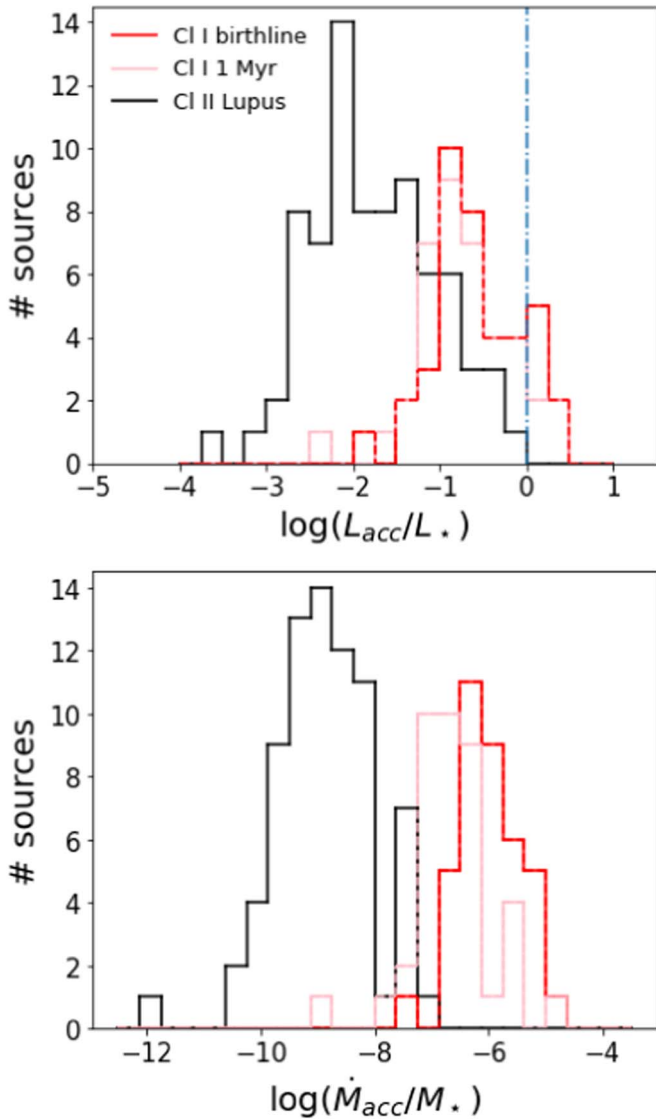


Figure 2. Histograms of the ratios L_{acc}/L_* (top panel) and \dot{M}_{acc}/M_* (bottom panel) for Class I assuming the age of the birthline (red) and 1 Myr (pink) compared to the histogram of the same quantity for the Class II sample of the Lupus star-forming region. The blue dashed-dotted line corresponds to $L_{\text{acc}}/L_* = 1$.

and only two of them have a low veiling value, showing that the accretion luminosity and the veiling are related, as already noted in previous works (e.g., Calvet et al. 2004; Fischer et al. 2011; Fiorellino et al. 2021).

We note that it is only for 15 out of 39 young stars (38%) that the accretion luminosity has a value compatible with the condition of being the main contribution to the bolometric luminosity, even if $L_{\text{acc}}/L_* \gg 1$ is what is expected for Class I protostars in general. We think this result shows the above-mentioned bias in our sample. This strongly suggests that our conclusions are not meant to be intended for Class I objects in general, but only for the less embedded Class I YSOs for which it was possible to estimate the veiling.

3.4. Disk Dust Masses

For the overall sample described in Section 2 we searched for (sub)millimeter fluxes, finding suitable observations for only 60 of them. We searched for the coordinates and the

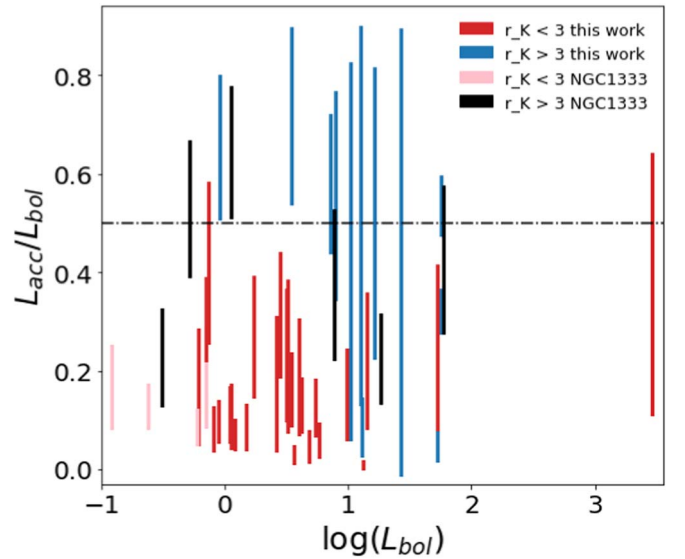


Figure 3. The ratio $L_{\text{acc}}/L_{\text{bol}}$ as a function of the bolometric luminosity for Class I with veiling smaller than three (red) and higher than three (blue). We compare our results with Class I in the Perseus NGC 1333 cluster for low-veiled (pink) and high-veiled (black) sources.

names of sources across the literature and the archival interferometric data. We included a dust mass measurement in our analysis if the flux measurement was available at $<1''$ resolution to mitigate the possible contribution from the envelope. In the subarcsecond regime with size of the beam comparable to the disk size, the envelope contribution is usually negligible, especially for the Class I systems where the envelope is largely dissipated (Tychoniec et al. 2020). We collected data on dust disk fluxes for 21 sources from Table 1, for 12 sources from Table 2, and for all the sources in Table 3. Appendix D contains millimeter fluxes and references for all the sources.

From the flux density (F_ν) we calculated the dust mass by inverting the modified blackbody equation:

$$M_{\text{dust}} = \frac{d^2 F_\nu}{\kappa_\nu(\beta) B_\nu(T_{\text{dust}})}, \quad (2)$$

where d is the distance to the source, B_ν is the Planck function for the dust temperature T_{dust} , and κ_ν is the dust opacity at the frequency of the observation ν . The equation is accurate for optically thin emission, otherwise it provides a lower limit on the dust mass measurement.

A dust temperature of 30 K is assumed, as is typically assumed for embedded young stars (i.e., Ansdell et al. 2016). If the temperature is lower, similarly to Class II disks, the total dust mass would be higher. We adopted a dust opacity value of $0.00899 \text{ g cm}^{-2}$ (Ossenkopf & Henning 1994) and a spectral emissivity slope $\beta=1$. With uniform assumptions on dust properties we are not introducing additional discrepancy between the disks measured within different observing projects.

We are aware that there is no agreement on the accuracy of the disk mass estimation (see the on-going debate in Miotello et al. 2022, Manara et al. 2022, and references therein). In brief, some studies suggest a severe underestimation of the disk mass because of the optical thickness or dust scattering (Zhu et al. 2019). In contrast, Sheehan et al. (2022) show that protostellar disk dust masses can be overestimated by using the isothermal disk assumption, and this effect is higher the less massive are

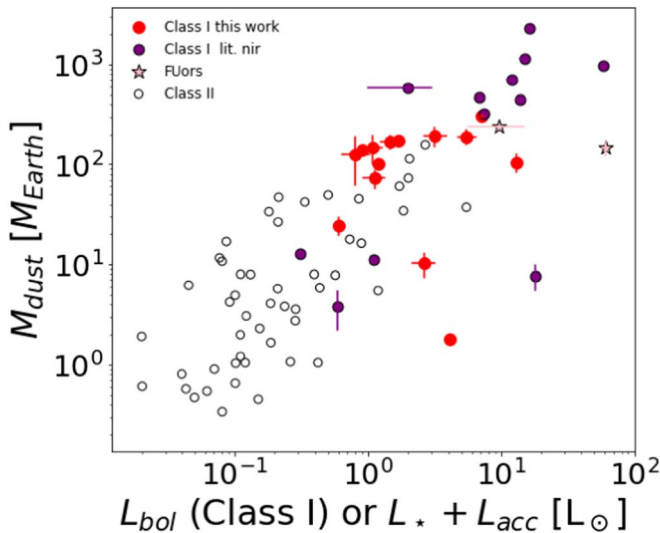


Figure 4. Disk dust mass as a function of bolometric luminosity for the sample of Class I sources in Tables 2 (purple dots) and 4 (red dots), and for FUors in Table 1 that have disk estimates. For Class II, the disk mass is plotted against the sum of stellar and accretion luminosity. The big empty red circle highlights source ID 02, for which no photometry at $\lambda > 100 \mu\text{m}$ was available and therefore L_{bol} is probably underestimated. Other sources with the same issue are not shown in this plot since we do not provide M_{dust} estimates for them.

the disks. These two opposite effects would increase the spread of disk masses. In other words, more massive disks would be even more massive while the low-mass end would be even less massive.

Figure 4 presents disk masses calculated for our sample of Class I (red dots) and FUors (pink stars), for other Class I present in the literature (purple dots), and for Class II of Lupus (empty circles). Class I young stars follow the same trend as Class II, extending the linear distribution of Class II in the upper right part of the plot, which shows that M_{disk} is higher in Class I than in Class II. We note that the population of FUors seems to deviate from this general trend. Kóspál et al. (2021) found that FUors have larger disk masses than either regular Class I or Class II objects. A possible explanation for this might be that FUor disks are also smaller and more optically thick, so by using the optically thin assumption as we did (by converting the continuum fluxes to disk masses), we underestimated the dust mass in FUors more severely than for regular disks. However, the significance of this deviation cannot be established with only three sources, and further data and more accurate analysis are needed to confirm the hint suggested by this figure.

4. Discussion

4.1. Accretion Properties versus Stellar Properties

The relations between the accretion and stellar luminosity, and the mass accretion rate and the stellar mass, are well established for CTTS (see Manara et al. 2022, and references therein). The same relations have been investigated recently for Class I YSOs by Fiorellino et al. (2021). They show that Class I of the NGC 1333 cluster have higher \dot{M}_{acc} than Class II of the same cluster with similar stellar mass. While this result is demonstrated for the NGC 1333 cluster, further observations are needed to see whether this conclusion is valid for other star-forming regions and/or in general for Class I objects.

Figure 5 (left panel) shows the accretion luminosity as a function of the stellar luminosity for our sample of Class I (red

and blue dots depending on the veiling) and for Class I of NGC 1333 (pink and black segments depending on the veiling). We plot also the Class II samples of Lupus and NGC 1333 (empty circles), as a comparison. The accretion luminosity in our sample ranges between 0.03 and $1263 L_{\odot}$ for stellar luminosity between 0.28 and $3.65 L_{\odot}$. This figure shows that the less veiled sources (red filled circles) are compatible with the Class II trend, while the most veiled sources are the ones that deviate the most from the Class II fit to higher values of L_{acc} for $L_{\star} < 1 L_{\odot}$. This veiling-dependent trend is valid also for the Class I population of NGC 1333 (pink and black lines in the plot). We note that the Class II NGC 1333 fit (gray dotted-dashed line) reproduces the low-veiled Class I distribution better than the Class II Lupus fit does (gray solid line), while the high-veiled Class I objects represent the subsample with the wider spread in this plot.

We also plotted the distribution of \dot{M}_{acc} versus M_{\star} in Figure 5 (right panel). The mass accretion rate of our sample ranges between $\log(\dot{M}_{\text{acc}}/M_{\odot} \text{ yr}^{-1}) = -8.41$ and -3.48 for stellar masses between 0.13 and $3.06 M_{\odot}$. In this plot, the Class I sample is not in agreement with the Class II trend, and shows higher accretion values than the Class II with similar stellar mass. The most veiled sources are accreting more than less veiled YSOs with similar mass, with the exception of two stars more massive than $1 M_{\odot}$. We note that for both the L_{acc} versus L_{\star} and the \dot{M}_{acc} versus M_{\star} distributions, the only source that lies below the trend of Class II YSOs (gray band) is a source for which photometry at $\lambda > 100 \mu\text{m}$ was not available. Therefore, in this case, it should be considered that the bolometric luminosity we provide is underestimated, and the accretion luminosity is potentially higher.

The assumption on the age results in a large uncertainty (displayed in the plots by the line that links the birthline and 1 Myr results for each source), in particular in M_{\star} . This prevents us from fitting the \dot{M}_{acc} versus M_{\star} distribution of Class I YSOs. We plot a linear relation with a unitary slope (black dashed line) to guide the reader in observing that the Class I sample seems to present a flatter distribution than the Class II sources, whose slope is about 2 (2.1 ± 0.2 in particular for Lupus, Fiorellino et al. 2021). We attempted some fits considering the same age for the overall sample. Assuming that all the sources are on the birthline, we obtained $\log \dot{M}_{\text{acc}} = (1.64 \pm 0.40) \log M_{\star} + (-5.63 \pm 0.21)$, and by assuming they are all 1 Myr old, we found $\log \dot{M}_{\text{acc}} = (0.59 \pm 0.27) \log M_{\star} + (-6.64 \pm 0.12)$. We stress that these fits are not reliable, since we do not know the exact age of each source, but can be seen as possible extremes, considering that at least some objects are probably younger. It is interesting that by assuming the oldest age for the overall sample, the intercept value is -6.64 ± 0.12 , larger than for Lupus (-8.2 ± 0.10 , Fiorellino et al. 2021) and compatible within the error with the intercept of the NGC 1333 sample (-7.3 ± 0.6 , Fiorellino et al. 2021), whose age is estimated to be ~ 1 Myr.

The mass accretion rate is predicted to correlate with the disk mass. This is predicted by viscous models (e.g., Hartmann et al. 1998; Lodato et al. 2017; Rosotti et al. 2017) and MHD wind models (e.g., Tabone et al. 2022). This correlation was indeed observed for Class II YSOs (Manara et al. 2016). The data presented here allow a similar exploration of this relation in the Class I phase on a statistically significant sample. We refer the reader to the dedicated letter (Fiorellino et al. 2022) where we studied the \dot{M}_{acc} versus M_{disk} distribution, comparing Class I and Class II samples.

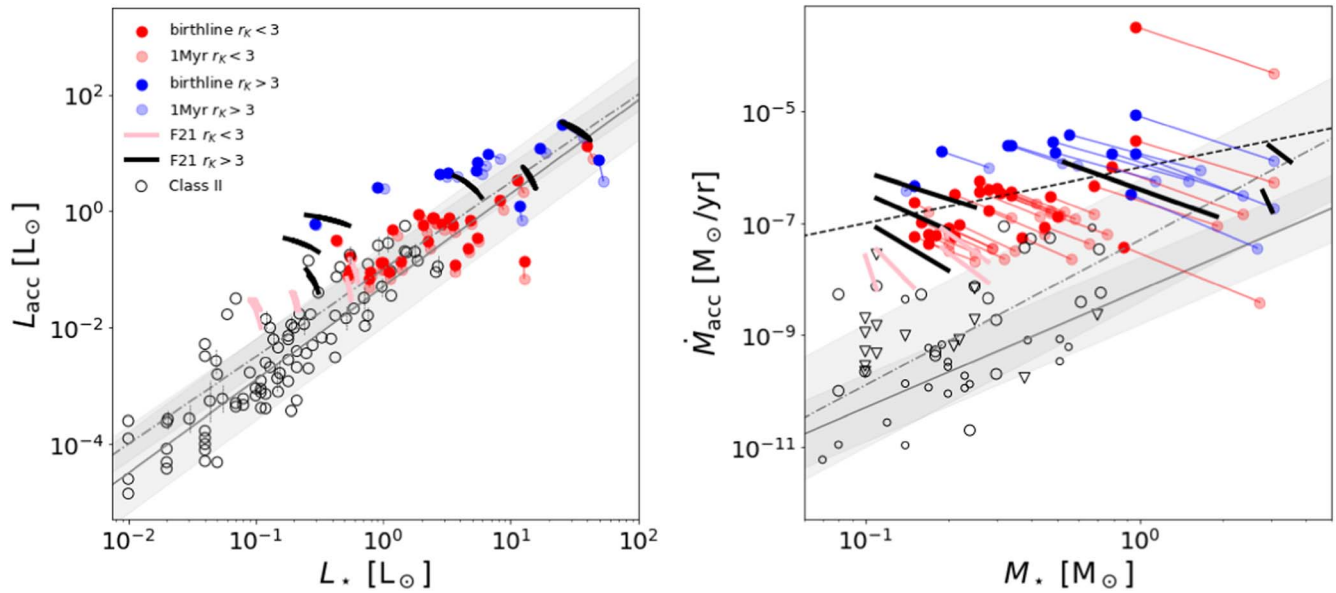


Figure 5. Left: accretion luminosity vs. stellar luminosity. Red and blue dots are Class I with $r_K < 3$ and $r_K > 3$, respectively, and are blurred depending on the assumed age as described in the legend. Source for which photometry at $\lambda > 100 \mu\text{m}$ is not available are surrounded by big red/blue empty circles. The two values (birthline and 1 Myr) are linked by a line to show that all the combinations of accretion and stellar parameters between the two dots are possible. Similarly, the ranges of possible parameters assuming the age between the birthline and 1 Myr are shown for the NGC 1333 cluster depending on the veiling, pink for $r_K > 3$ and black for $r_K < 3$. Empty black circles are Class II of Lupus and Perseus NGC 1333 clouds, and triangles showed the related upper limits. The solid and dotted–dashed lines are the best fit of the Lupus and NGC 1333 Class II, respectively (Fiorellino et al. 2021). The gray region corresponds to the standard deviation of the fits. Right: mass accretion rate vs. stellar mass. All the symbols are as in the left panel. The dashed–dotted black line shows $\log \dot{M}_{\text{acc}} \propto \log M_*$.

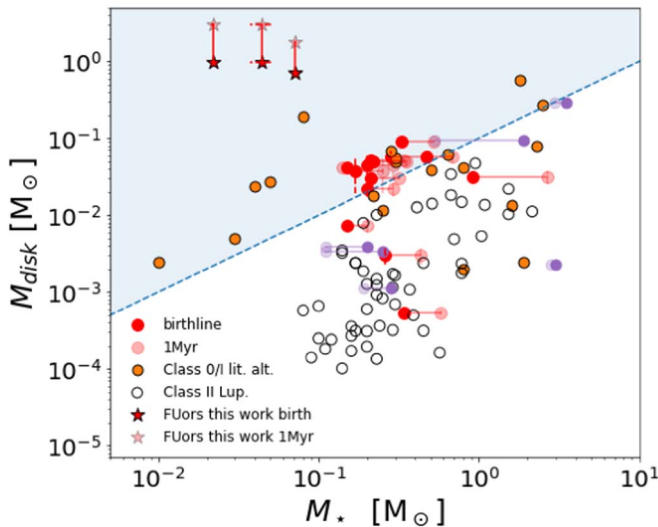


Figure 6. Disk mass vs. stellar mass. Red dots are our Class I results assuming they are on the birthline; the pink dots are the same sources’ results assuming they are 1 Myr old. Big empty red circles highlight source ID 02, for which no photometry at $\lambda > 100 \mu\text{m}$ was available. Other sources with the same issue are not shown in this plot since we do not provide M_{dust} estimates for them. Purple dots are sources in Table 2, where blurring indicates the age for the NGC 1333 sources, as described in the main text. Orange dots are sources in Table 3. Red stars are FUors from Appendix B. The blue dashed line marks the region of the disk instability regime $M_{\text{disk}} > 0.1 M_*$, filled in light blue.

4.2. Stellar Mass versus Disk Mass

In Figure 6 we show the stellar mass of the protostars compared with their disk mass. Class I have systematically larger disk mass than Lupus Class II stars, as expected from the evolutionary path.

The M_{disk} versus M_* distribution of Class I samples is flat compared with the steeper slope for Class II systems. The

evolution of this trend for Class II has been studied in previous works (e.g., Pascucci et al. 2016; Ansdell et al. 2017; Testi et al. 2022), which concluded that the slope becomes steeper with time. Therefore, our finding is consistent with this trend.

Models of early disk formation and evolution suggest rapid change of the M_{disk} versus M_* relation in the first 0.1 Myr of system evolution (Hennebelle et al. 2020). Therefore the low ratio seen for only young sources is consistent and suggests extreme youth of those systems.

An open question regarding accretion is how much the episodic accretion is statistically important in the star formation process, since the list of eruptive objects is nowadays confined to about 50 sources at different evolutionary stages (Fischer et al. 2022). According to the current scenario of eruptive accretion, the disk instability is fundamental in triggering the extremely strong outbursts of FUors and EXors. Therefore, it makes sense to look for hints of disk instability in “steady” accretors. Signatures of disk fragmentation and other effects of instability in the young disks have been observed in several works (e.g., Tobin et al. 2016b; Alves et al. 2019). Thanks to the sensitive observations, new techniques can even trace a past outburst by studying the ice-line radius or the presence of outburst tracers (see Fischer et al. 2022, and references therein). Indeed, Kóspál et al. (2021) found that about 2/3 of FUors in their study may have a gravitationally unstable disk, which can cause the typical strong outbursts.

Motivated by this, we checked in Figure 6 the stability of the disks in our Class I sample (including some FUors). We plot a blue dashed line that represents the edge of the disk instability regime (light blue region), where $M_{\text{disk}} > 0.1 M_*$ (Equation (3) in Kratter & Lodato 2016). The plot shows that 81% (17 out of 21) of the sources in our sample, 75% (9 out of 12) of sources in Table 2 (purple dots), and 78% (21 out of 27) of sources in Table 3 (orange dots) lie in the light blue region. This means that while all Class II disks appear stable, the majority of

Table 4
Computed Distance, Bolometric Luminosity, Br γ Flux, and Dust Mass of the Sample in Table 1

ID	Name	Cloud	Distance (pc)	L_{bol} (L_{\odot})	$F_{\text{Br}\gamma}$ ($\text{erg s}^{-1} \text{cm}^{-2}$)	M_{dust} (M_{\oplus})
01	CG2010 IRAS 032203035N	Per-IC348	219.8 \pm 16.2 ^a	1.47 ^{0.26} _{0.21}	(4.25 \pm 1.34) $\times 10^{-15}$	168 \pm 25
02	2MASS J033312843121241	Per-IC348	319.5 \pm 23.7 ^a	5.43 ^{0.99} _{0.68} [†]	(5.69 \pm 7.06) $\times 10^{-16}$	190 \pm 28
03	IRAS 035073801	Per-B1	310.9 \pm 22.8 ^a	4.81 ^{0.75} _{0.64}	(2.92 \pm 3.45) $\times 10^{-15}$...
04*	NAMEIRA S041082803A	Tau-L1495	170.1 \pm 24.9 ^a	0.30 ^{0.11} _{0.08} [†]	(5.14 \pm 1.91) $\times 10^{-15}$...
05	BHS98 MHO1	Tau-L1495	134.0 \pm 7.0 ^a	1.69 ^{0.14} _{0.16}	(7.10 \pm 0.89) $\times 10^{-14}$	171 \pm 18
06	BHS98 MHO2	Tau-L1495	131.0 \pm 2.9 ^a	1.20 ^{0.05} _{0.05}	(3.00 \pm 0.93) $\times 10^{-14}$	101 \pm 5
07	IRAS 041692702	Tau-L1495	129.5 \pm 12.9 ^b	1.09 ^{0.19} _{0.21}	(1.97 \pm 0.40) $\times 10^{-15}$	147 \pm 47
08*	MDM2001 CFHT BDTau19	Tau-B213	155.9 \pm 15.6 ^b	0.63 ^{0.14} _{0.10}	(2.27 \pm 0.63) $\times 10^{-15}$	7.2 \pm 1.5
09	NAMEIRA S041812654B	Tau-B213	155.9 \pm 15.6 ^b	0.74 ^{0.17} _{0.13}	(2.58 \pm 0.13) $\times 10^{-15}$...
10	VFS Tau	Tau-Aur	133.9 \pm 2.4 ^a	4.15 ^{0.10} _{0.16}	(3.56 \pm 0.51) $\times 10^{-14}$	1.8 \pm 0.1
11	2MASS J042200692657324	Tau-Aur	133.9 \pm 2.4 ^z	0.90 ^{0.05} _{0.08}	(4.20 \pm 0.32) $\times 10^{-15}$	97 \pm 10
12*	VDG Tau	Tau-Aur	125.3 \pm 1.9 ^a	3.89 ^{0.11} _{0.16}	(6.35 \pm 0.25) $\times 10^{-13}$	325 \pm 11
13	IRAS 042482612	Tau-B213	155.9 \pm 15.6 ^b	0.69 ^{0.14} _{0.09}	(6.53 \pm 1.19) $\times 10^{-15}$...
14*	Haro 613	Tau-Aur	128.6 \pm 1.6 ^a	1.08 ^{0.03} _{0.03}	(9.77 \pm 1.26) $\times 10^{-14}$	200 \pm 5
15	IRAS 042952251	Tau-L1546	160.76 \pm 16.1 ^b	0.81 ^{0.21} _{0.16}	(2.81 \pm 0.73) $\times 10^{-15}$	125 \pm 62
16	IRAS 043153617	California	359.4 \pm 24.7 ^a	3.44 ^{0.46} _{0.46}	(8.98 \pm 0.60) $\times 10^{-14}$...
17	IRAS 043812540	Tau-L1527	141.8 \pm 1.4 ^b	0.60 ^{0.03} _{0.02}	(2.94 \pm 0.55) $\times 10^{-15}$	25 \pm 5
18	VV347 Aur	Tau-Aur	206.6 \pm 2.3 ^a	3.49 ^{0.14} _{0.10}	(7.88 \pm 1.03) $\times 10^{-14}$...
19*	IRAS 045910856	ONC A	400 \pm 40 ^c	2.95 ^{1.69} _{1.25}	(4.10 \pm 1.34) $\times 10^{-13}$...
20	IRAS 052890430	ONC A	400 \pm 40 ^c	7.78 ^{1.55} _{1.52}	(1.71 \pm 0.17) $\times 10^{-14}$...
21	2MASS J053332510629441	ONC A	390 \pm 39 ^c	14.0 ^{5.7} _{4.2}	(1.03 \pm 0.12) $\times 10^{-14}$...
22	Parentago 2649	ONC A	398.5 \pm 2.5 ^a	12.9 ^{0.3} _{0.2}	(2.03 \pm 0.57) $\times 10^{-15}$	105 \pm 21
23	Haro 590	ONC B	416.4 \pm 7.8 ^a	9.74 ^{1.49} _{1.41}	(4.29 \pm 0.44) $\times 10^{-14}$...
24	2MASS J054006370038370	ONC B	408.2 \pm 12.4 ^a	0.87 ^{0.05} _{0.06} [†]	(5.23 \pm 0.92) $\times 10^{-15}$...
25	2MASS J054005790038429	ONC B	421.9 \pm 10.7 ^a	2.76 ^{0.17} _{0.17} [†]	(3.99 \pm 0.19) $\times 10^{-14}$...
26	2MASS J054020540756398	ONC A	427.2 \pm 72.1 ^a	10.4 ^{3.7} _{4.1}	(4.66 \pm 0.25) $\times 10^{-14}$...
27	MB 9154	ONC A	502.6 \pm 183.3 ^a	0.60 ^{0.51} _{0.40} [†]	(4.47 \pm 0.83) $\times 10^{-15}$...
28	2MASS J054050590805487	ONC A	440 \pm 44 ^c	1.12 ^{0.20} _{0.20}	(1.93 \pm 0.40) $\times 10^{-15}$	72 \pm 15
29	2MASS J054049910806084	ONC A	440 \pm 44 ^c	2.63 ^{0.52} _{0.46}	(3.98 \pm 0.57) $\times 10^{-15}$	10 \pm 3
30	IRAS 054050117	ONC B	420 \pm 42 ^c	3.18 ^{0.71} _{0.56}	(1.02 \pm 0.15) $\times 10^{-14}$	192 \pm 39
31	IRAS 054270116	ONC B	420 \pm 42 ^c	13.2 ^{2.5} _{3.1} [†]	(4.68 \pm 0.95) $\times 10^{-16}$...
32*	VV1818 Ori	Orion	633.4 \pm 22.7 ^a	292 ¹⁹ ₁₈	(3.50 \pm 0.55) $\times 10^{-13}$	58 \pm 4
33	2MASS J055749461405278	Orion	466.0 \pm 44.6 ^a	12.44 ^{1.97} _{1.96}	(1.93 \pm 0.09) $\times 10^{-14}$...
34	2MASS J055749181406080	Orion	1039.5 \pm 334.4 ^a	5.73 ^{1.17} _{0.93} [†]	(2.07 \pm 0.54) $\times 10^{-15}$...
35*	WL 16	Oph	138.4 \pm 2.6 ^d	15.05 ^{1.13} _{1.28}	(2.53 \pm 0.11) $\times 10^{-13}$	3.7 \pm 0.2
36	CG2010 IRAS 162882450W1	Oph	138.4 \pm 2.6 ^d	0.009 ^{0.001} _{0.001} [†]	(8.25 \pm 1.30) $\times 10^{-14}$...
37*	IRAS 162894449	Sa 187	350.3 \pm 2.5 ^e	60.5 ^{3.0} _{2.7}	(1.24 \pm 0.19) $\times 10^{-13}$	146 \pm 16
38	JCMSTF J1634294154700	L43	160 \pm 16 ^f	3.63 ^{0.72} _{0.50}	(1.31 \pm 0.54) $\times 10^{-14}$...
39	2MASS J164658260935197	L260	322.09 \pm 9.7 ^e	3.15 ^{0.23} _{0.15}	(5.38 \pm 1.05) $\times 10^{-15}$...
40	IRAS 182750040	Serpens	383.1 \pm 12.2 ^a	16.2 ^{1.1} _{1.0}	(6.28 \pm 0.98) $\times 10^{-14}$...
41*	2MASS J183646330110294	Serpens	580.4 \pm 70.6 ^a	63.8 ^{20.0} _{16.1}	(8.39 \pm 3.75) $\times 10^{-15}$...
42	VS CrA	CrA	160.5 \pm 1.8 ^a	7.13 ^{0.20} _{0.21}	(9.83 \pm 0.45) $\times 10^{-13}$	307 \pm 7
43*	Parsamian 21	Aquila	400 \pm 100 ^g	9.7 ^{3.96} _{4.99}	(1.01 \pm 0.30) $\times 10^{-15}$	214 \pm 107
44	LDN 1100	Cepheus	561.8 \pm 107.8 ^a	26.52 ^{13.03} _{8.40} [†]	(4.80 \pm 0.92) $\times 10^{-15}$...
45	IRAS 214455712	IC 1396 East	360 \pm 36 ^h	52.48 ^{23.23} _{14.67}	(2.10 \pm 1.16) $\times 10^{-15}$...
46	IRAS 222666845	L1221, HH 363	200 \pm 20 ⁱ	2.61 ^{0.50} _{0.58}	(4.87 \pm 0.76) $\times 10^{-15}$...
47	IRAS 222726358B	L1206	950.0 \pm 95 ⁱ	53.0 ^{8.7} _{7.7} [†]	(5.44 \pm 0.68) $\times 10^{-14}$...
48	EMLkHA 233	Lacerta	498.9 \pm 11.6	56.1 ^{2.1} _{3.6}	(1.51 \pm 0.18) $\times 10^{-14}$...
49	2MASS J230549766230011	Cep C	1190 \pm 119 ^h	2882 ⁴⁵⁵ ₇₂₉	(2.95 \pm 0.33) $\times 10^{-14}$...
50	2MASS J000143254805189	Cepheus	379.9 \pm 15.6 ^a	4.01 ^{0.55} _{0.39}	(8.02 \pm 1.26) $\times 10^{-15}$...

Notes. ^aParallax distance with Gaia EDR3 direct match (Gaia Collaboration et al. 2021), Distance to the region (error is set to 10% if not stated in the literature); ^bKrolikowski et al. (2021), ^cTobin et al. (2020), ^dOrtiz-León et al. (2018), ^eZari et al. (2018), ^fAnglada & Rodríguez (2002), ^gKóspál et al. (2008), ^hWouterloot & Brand (1989), ⁱHilton & Lahulla (1995), ^jassumed to be the same as FS TauA where Gaia EDR3 is available, ^kdistance estimated using photogeometric method from Gaia EDR3 data Bailer-Jones et al. (2020). [†] L_{bol} of YSOs for which no photometry at $\lambda > 100 \mu\text{m}$ was available.

Table 5
Stellar and Accretion Parameters of the 39 Class I Protostars from Connelley & Greene (2010) Computed in This Work

ID	Age	A_V (mag)	L_{acc} (L_{\odot})	L_{\star} (L_{\odot})	T_{eff} (K)	M_{\star} (M_{\odot})	R_{\star} (R_{\odot})	$\log \dot{M}_{\text{acc}}$ ($M_{\odot} \text{ yr}^{-1}$)
01	BL-1 Myr	18.61-15.95	0.14-0.10	1.36-1.40	3126-3487	0.22-0.35	4.00-3.05	-7.03/ -7.49
02	BL-1 Myr	29.21-28.02	0.71-0.61	4.87-4.97	3673-3958	0.47-0.68	5.35-4.43	-6.52/ -6.83
03	BL-1 Myr	23.15-21.94	0.23-0.20	4.64-4.67	3652-3935	0.45-0.65	5.31-4.42	-7.06/ -7.36
05	BL-1 Myr	15.69-13.61	0.49-0.39	1.19-1.29	3073-3467	0.21-0.34	3.75-3.04	-6.48/ -6.90
06	BL-1 Myr	9.93-7.71	0.09-0.07	1.11-1.13	3090-3407	0.21-0.32	3.72-2.96	-7.23/ -7.63
07	BL-1 Myr	41.51-39.76	0.13-0.10	0.95-0.98	3020-3313	0.20-0.29	3.50-2.77	-7.08/ -7.44
09	BL-1 Myr	20.39-19.99	0.32-0.31	0.43-0.44	2834-2936	0.15-0.17	3.00-2.35	-6.62/ -6.78
10	BL-1 Myr	21.65-19.50	0.58-0.44	3.54-3.68	3448-3868	0.34-0.58	4.82-4.11	-6.50/ -6.92
11	BL-1 Myr	43.04-43.04	0.60-0.59	0.29-0.30	2818-2835	0.15-0.14	3.01-2.26	-6.32/ -6.41
13	BL-1 Myr	27.45-26.68	0.17-0.16	0.55-0.56	2851-3040	0.16-0.20	3.08-2.51	-6.97/ -7.19
15	BL-1 Myr	28.29-26.67	0.07-0.05	0.77-0.78	2917-3200	0.17-0.25	3.14-2.64	-7.36/ -7.67
16	BL-1 Myr	2.63-1.99	2.54-2.44	0.90-1.01	2972-3264	0.19-0.28	3.50-2.82	-5.72/ -6.00
17	BL-1 Myr	36.77-35.70	0.08-0.07	0.53-0.54	2834-3037	0.15-0.20	3.00-2.48	-7.23/ -7.49
18	BL-1 Myr	8.96-6.78	0.62-0.48	2.89-3.03	3388-3780	0.31-0.51	4.67-3.84	-6.46/ -6.88
20	BL-1 Myr	27.81-26.81	4.54-3.98	3.25-3.80	3413-3849	0.34-0.59	4.77-4.06	-5.60/ -5.97
21	BL-1 Myr	30.49-26.48	3.41-2.11	11.39-12.69	3960-5029	0.79-2.37	6.45-4.38	-5.99/ -6.84
22	BL-1 Myr	15.20-10.33	1.25-0.70	11.72-12.27	4050-5158	0.92-2.67	6.86-4.03	-6.48/ -7.44
23	BL-1 Myr	6.51-4.12	1.52-1.09	8.26-8.70	3890-4722	0.68-1.91	6.07-4.21	-6.33/ -7.04
24	BL-1 Myr	4.88-3.58	0.09-0.08	0.79-0.80	2951-3217	0.18-0.25	3.29-2.63	-7.22/ -7.53
25	BL-1 Myr	3.97-2.62	0.89-0.75	1.88-2.02	3236-3630	0.26-0.42	4.45-3.41	-6.24/ -6.64
26	BL-1 Myr	12.89-11.04	4.90-4.30	5.36-5.96	3563-4187	0.49-1.14	5.31-4.20	-5.74/ -6.24
27	BL-1 Myr	4.72-3.75	0.10-0.09	0.55-0.57	2919-3051	0.17-0.20	3.26-2.48	-7.20/ -7.39
28	BL-1 Myr	17.36-15.57	0.13-0.10	0.99-1.02	3020-3331	0.20-0.29	3.50-2.86	-7.09/ -7.44
29	BL-1 Myr	23.28-21.00	0.59-0.45	2.07-2.21	3255-3652	0.26-0.43	4.46-3.46	-6.43/ -6.87
30	BL-1 Myr	16.21-14.04	0.78-0.61	2.48-2.65	3312-3715	0.28-0.47	4.56-3.66	-6.38/ -6.81
31	BL-1 Myr	32.89-27.37	0.14-0.07	12.71-12.78	4027-5188	0.87-2.73	6.71-4.19	-7.42/ -8.41
33	BL-1 Myr	20.70-18.35	6.99-6.05	5.46-6.40	3548-4371	0.48-1.50	5.28-3.68	-5.54/ -6.23
34	BL-1 Myr	18.50-17.15	0.35-0.30	5.50-5.55	3716-4028	0.50-0.76	5.43-4.57	-6.88/ -7.20
38	BL-1 Myr	17.66-15.55	0.12-0.09	3.62-3.65	3509-3846	0.37-0.56	4.96-4.05	-7.25/ -7.64
39	BL-1 Myr	28.21-26.36	0.77-0.63	2.42-2.56	3349-3715	0.30-0.47	4.64-3.66	-6.37/ -6.77
40	BL-1 Myr	21.99-19.73	9.53-8.01	6.64-8.16	3684-4517	0.55-1.65	5.53-4.12	-5.41/ -6.05
42	BL-1 Myr	6.77-5.79	4.34-3.99	2.78-3.14	3410-3781	0.33-0.52	4.79-3.86	-5.60/ -5.93
44	BL-1 Myr	40.07-36.23	11.83-9.94	16.99-18.89	3940-5088	0.79-2.36	6.42-4.86	-5.75/ -6.50
45	BL-1 Myr	53.39-46.30	7.65-3.35	49.12-53.42	4074-5754	0.96-3.06	7.02-5.69	-5.76/ -6.72
46	BL-1 Myr	30.71-28.37	0.31-0.23	2.26-2.33	3312-3673	0.28-0.45	4.56-3.52	-6.77/ -7.20
47	BL-1 Myr	6.59-3.61	13.27-8.05	39.26-44.48	4074-5754	0.96-3.06	7.02-5.69	-5.52/ -6.27
48	BL-1 Myr	40.58-36.44	29.99-18.03	25.29-37.26	4074-5754	0.96-3.06	7.02-5.69	-5.06/ -5.88
49	BL-1 Myr	47.24-42.53	1263-797	1482-1948	4074-5754	0.96-3.06	7.02-5.69	-3.48/ -4.31
50	BL-1 Myr	20.17-18.40	0.79-0.64	3.30-3.45	3448-3802	0.34-0.53	4.82-3.91	-6.42/ -6.80

protostars show evidence of gravitationally unstable disks, suggesting that these sources experience some strong outbursts at some point during their evolution.

We note that all the FUors do not lie in the instability region, as supposed for eruptive sources. We think that this is because we analyzed our FUors assuming their disks were optically thin, thus underestimating their disk mass. The results in this paper confirm that this method is not suitable for determining the parameters of FUors.

Since the sources in our sample are known to have gravitationally stable disks, we looked for signatures of past or future outbursts. We checked whether our sources were analyzed in Hsieh et al. (2019b), where they looked for N_2H^+ as a tracer of a recent outburst. Among our sources in Table 1, only 2MASS J03331284+3121241 has been studied. They found no clear detection for this star, thus they suggested that the envelope has pretty much dissipated. Because it lies in the instability region of Figure 6, we can speculate this source will

experience a future outburst. Concerning young stars in Tables 2 and 3, four objects were observed by Hsieh et al. (2019b): 2MASS J03283968+3117321, which shows very weak or no emission and therefore its envelope may have also dissipated; 2MASS J03285842+3122175 and 2MASSJ0329 0149+3120208, both stable according to our analysis; and V512 Per, whose $M_{\text{disk}}/M_{\star}$ ratio suggests it is stable, but it has been suggested that it is currently in outburst (Eisloffel et al. 1991). This would mean that V512 Per is one of the few young stars in outburst within the stability region (Kóspál et al. 2021) and thus its outburst must have been triggered by another physical process such as an interaction with its companion or a fly-by event (Vorobyov et al. 2021). Another possible explanation is that since we use the optically thin assumption, the disk mass is underestimated. In this case, a higher mass may shift it to the unstable region. However, our results show that a high fraction of Class I disks, like FUors, are gravitationally unstable.

5. Conclusions

We analyzed available data for a sample of Class I protostars composed of 50 YSOs from Connelley & Greene (2010, see Table 1), for which we computed an accurate estimate of the bolometric luminosity (see Table 4); for the first time, we provide the accretion and stellar parameters for 39 of them (Table 5). We also select 18 YSOs already analyzed with very similar methodologies to those we used in this work (see Table 2), and 27 YSOs studied with different methods (see Table 3). For the overall sample, we computed the disk dust mass, when archival interferometric data were available. In this way, we built the largest sample of accretion, disks, and stellar properties ever analyzed for protostars (Classes 0 and I). We briefly summarize the key conclusions of this work:

1. The accretion luminosity is higher in Class I than in Class II YSOs. This effect is smaller for the L_{acc} versus L_{\star} distribution of the low-veiled ($r_K < 3$) Class I objects. This highlights the crucial need for accurate veiling estimates for the accretion study of embedded YSOs
2. The mass accretion rate in Class I sources is systematically higher than in Class II. Although the uncertainty on the age prevents us from providing reliable a fit of our data, the \dot{M}_{acc} versus M_{\star} distribution of Class I appears flatter than the corresponding distribution for Class II objects.
3. The M_{disk} versus M_{\star} relation is flatter for young systems than for older ones. A large fraction of protostellar sources have the ratio $M_{\text{disk}}/M_{\star}$ above 0.1, suggestive of a propensity to gravitational instability.

Uniform samples of Class I and Class II protostars with identical initial conditions and the systematic analysis of more embedded sources are necessary to draw solid conclusions on the evolutionary path of YSOs and to be able to set the initial conditions for formation of stars and planets. As shown in Fiorellino et al. (2021), VLT/KMOS can be used on a wider range of sources. Future observations by JWST will deliver information on photospheres with NIRSpec and eventually enable the investigation of the protostellar accretion rates for even more embedded sources with MIRI.

We thank the anonymous referee for their useful comments. For this work we used ALMA archive data, we thus acknowledge 2016.1.01511.S, 2019.1.01813.S, and 2019.1.01792.S programs. This work has made use of data from the European Space Agency (ESA) mission Gaia (<https://www.cosmos.esa.int/gaia>), processed by the Gaia Data Processing and Analysis Consortium (DPAC), <https://www.cosmos.esa.int/web/gaia/dpac/consortium>. Funding for the DPAC has been provided by national institutions, in particular the institutions participating in the Gaia Multilateral Agreement. This project has received funding from the European Research Council (ERC) under the European Union’s Horizon 2020 Research & Innovation Programme under grant agreement No. 716155 (SACCRED) and by the European Union under the European Union’s Horizon Europe Research & Innovation Programme 101039452 (WANDA) and 101039651 (DiscEvol). Views and opinions expressed are, however, those of the author(s) only and do not necessarily reflect those of the European Union or the European Research Council. Neither the European Union nor the granting authority can be held responsible for them. G.R. acknowledges support from the Netherlands Organisation for Scientific Research (NWO, program No. 016.Veni.192.233) and from an STFC Ernest Rutherford Fellowship (grant No. ST/T003855/1). This work has been supported by the project PRIN-INAF 2019 “Spectroscopically Tracing the Disk Dispersal Evolution (STRADE).”

Appendix A Class II

In this appendix we will present the accretion rates and stellar parameters for those source that were classified as Class II after CG10 work, i.e., ID sources: 08, 12, 14, and 35.

These sources were analyzed by using the same routine we used for Class I but fixing the spectral type (from Connelley & Greene 2010) and setting the age as a free parameter. Results are listed in Table 6, and are compatible with typical accretion rates and stellar parameters of CTTS.

Table 6
Stellar and Accretion Parameters of the Class II Sources from CG10 Computed in This Work

ID	T_{eff} (K)	SpT	Age (yr)	A_V (mag)	L_{acc} (L_{\odot})	L_{\star} (L_{\odot})	M_{\star} (M_{\odot})	R_{\star} (R_{\odot})	$\log \dot{M}_{\text{acc}}$ ($M_{\odot} \text{ yr}^{-1}$)
08	5290	G7	2.09×10^7	14.80 ± 7.80	0.01 ± 0.01	0.51 ± 0.01	1.11 ± 0.01	1.20 ± 0.01	-9.31 ± 0.32
12	5740	G3	2.83×10^6	1.47 ± 1.00	0.77 ± 0.13	2.78 ± 0.13	1.48 ± 0.14	1.72 ± 0.21	-7.44 ± 0.08
14	5290	G7	2.09×10^7	2.43 ± 0.07	0.10 ± 0.02	0.88 ± 0.01	1.11 ± 0.01	1.20 ± 0.01	-8.39 ± 0.07
35	9230	A0	1.90×10^7	4.64 ± 0.36	0.52 ± 0.02	19.18 ± 0.02	2.14 ± 0.01	2.13 ± 0.01	-7.68 ± 0.02

Appendix B FUors

We report in Table 7 the results we get for FUors sources, even if we are aware that our method is unlikely to work for such objects.

Table 7
Stellar and Accretion Parameters of the FUors from Connelley & Greene (2010) Computed in This Work

ID	Age	A_V (mag)	L_{acc} (L_{\odot})	L_* (L_{\odot})	T_{eff} (K)	M_* (M_{\odot})	R_* (R_{\odot})	\dot{M}_{acc} ($M_{\odot} \text{ yr}^{-1}$)
04	BL-1 Myr	17-18	0.03-0.04	0.28-0.30	2818-2819	0.15-0.13	3.01-2.26	-7.65/ -7.71
19	BL-1 Myr	14-11	0.16-0.12	3.02-3.05	3396-3719	0.33-0.49	4.77-3.64	-7.07/ -7.48
32	BL-1 Myr	17-13	168-109	125-183	4074-5754	0.96-3.06	7.02-5.69	-4.32/ -5.11
37	BL-1 Myr	25-20	25-15	35-46	4074-5754	0.96-3.06	7.02-5.69	-5.17/ -6.03
41	BL-1 Myr	30-23	9.32-4.13	56-62	4074-5754	0.96-3.06	7.02-5.69	-5.65/ -6.61
43	BL-1 Myr	20-16	0.08-0.05	9.11-9.15	3852-4614	0.70-1.77	6.14-4.59	-7.67/ -8.31

Appendix C Spectral Energy Distribution

We present the spectral energy distributions of our sample in Figures 7, 8, and 9. We used the SEDBYS v.2.0 Python-based package (Davies 2021) to automatically look for the photometry available in published catalogs; data from these specific resources were reviewed and included in the SEDs: Beichman et al. (1988), Hillenbrand et al. (1992), Mannings & Emerson (1994), Cutri et al. (2003), Evans et al. (2003), Andrews & Williams (2007), Di Francesco et al. (2008), Abazajian et al. (2009), Ishihara et al. (2010), Yamamura et al. (2010), Bianchi et al. (2011), Ahn et al. (2012), Cutri et al. (2012), Page et al. (2012), Henden et al. (2015), Alam et al. (2015), Ribas et al. (2017), and Gaia Collaboration (2018).

In the following, we describe some interesting targets.

04108+2803A. Suggested to be a reddened Class II source in Furlan et al. (2008). Separated by $21''$ from its B component, 04108+2803B, which is much brighter in the IR. Source A is confirmed to be not detected longward of $100 \mu\text{m}$ in Herschel maps.

[MDM2001] CFHT-BD-Tau19. Classified as a brown dwarf. In Guieu et al. (2006) it presents a very rich spectrum with prominent accretion lines, including optical lines, hinting at a more evolved nature.

DG Tau A. Typically classified as a T Tauri star (Purser et al. 2018; Harrison et al. 2019). Index provided by Connelley & Greene (2010) consistent with Class II.

Haro 6-13. Based on Herschel photometry classified as Class II (Harrison et al. 2019).

2MASS J05405059-0805487, *2MASS J05404991-0806084*, *IRAS 05405-0117*. Based on Herschel photometry classified as flat-spectrum sources (Furlan et al. 2016).

2MASS J05333251-0629441. It is present in the SPIRE map but not listed in SPIRE Point Source Catalog. Shimajiri (2015) provides 1.1 mm flux.

IRAS16289-4449. It is present in the SPIRE map but not listed in SPIRE Point Source Catalog.

Parénago 2649. Nondetection in SPIRE map.

WL 16. Reclassified as Class II in Sadavoy et al. (2019) based on a saturated IR spectrum, detection of polycyclic aromatic hydrocarbons and weak outflow.

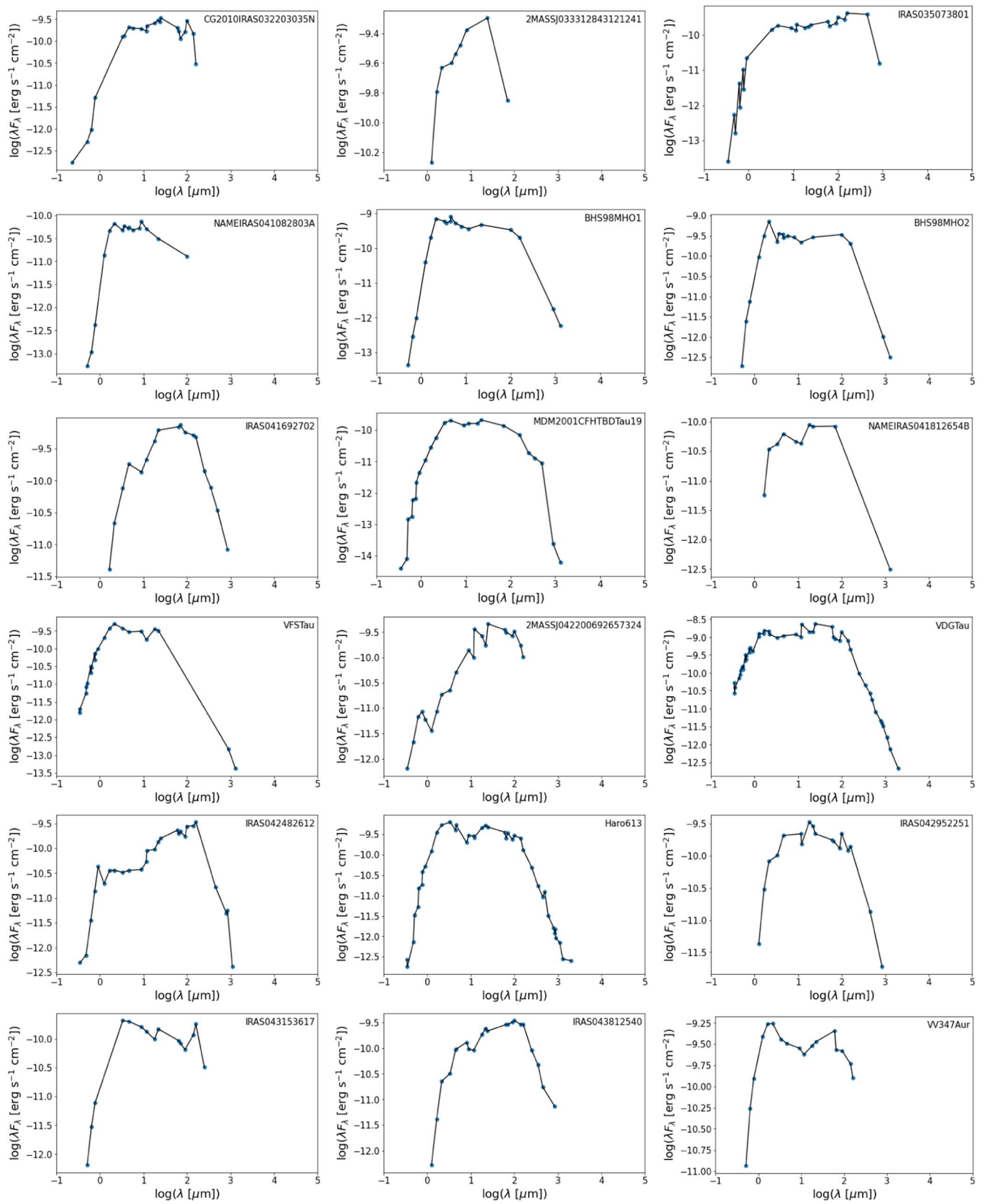


Figure 7. Spectral energy distributions of the YSOs.

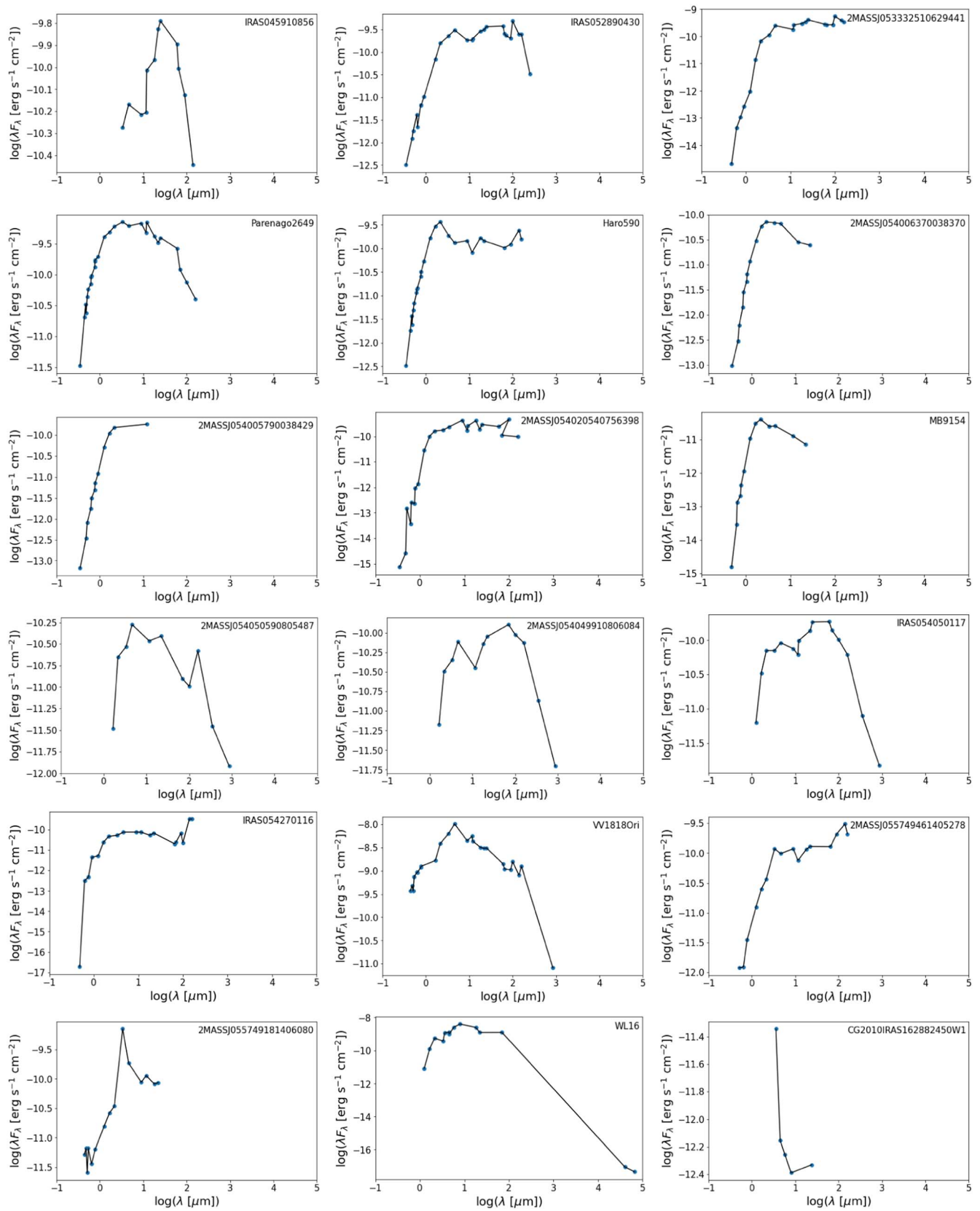


Figure 8. Spectral energy distributions of the YSOs.

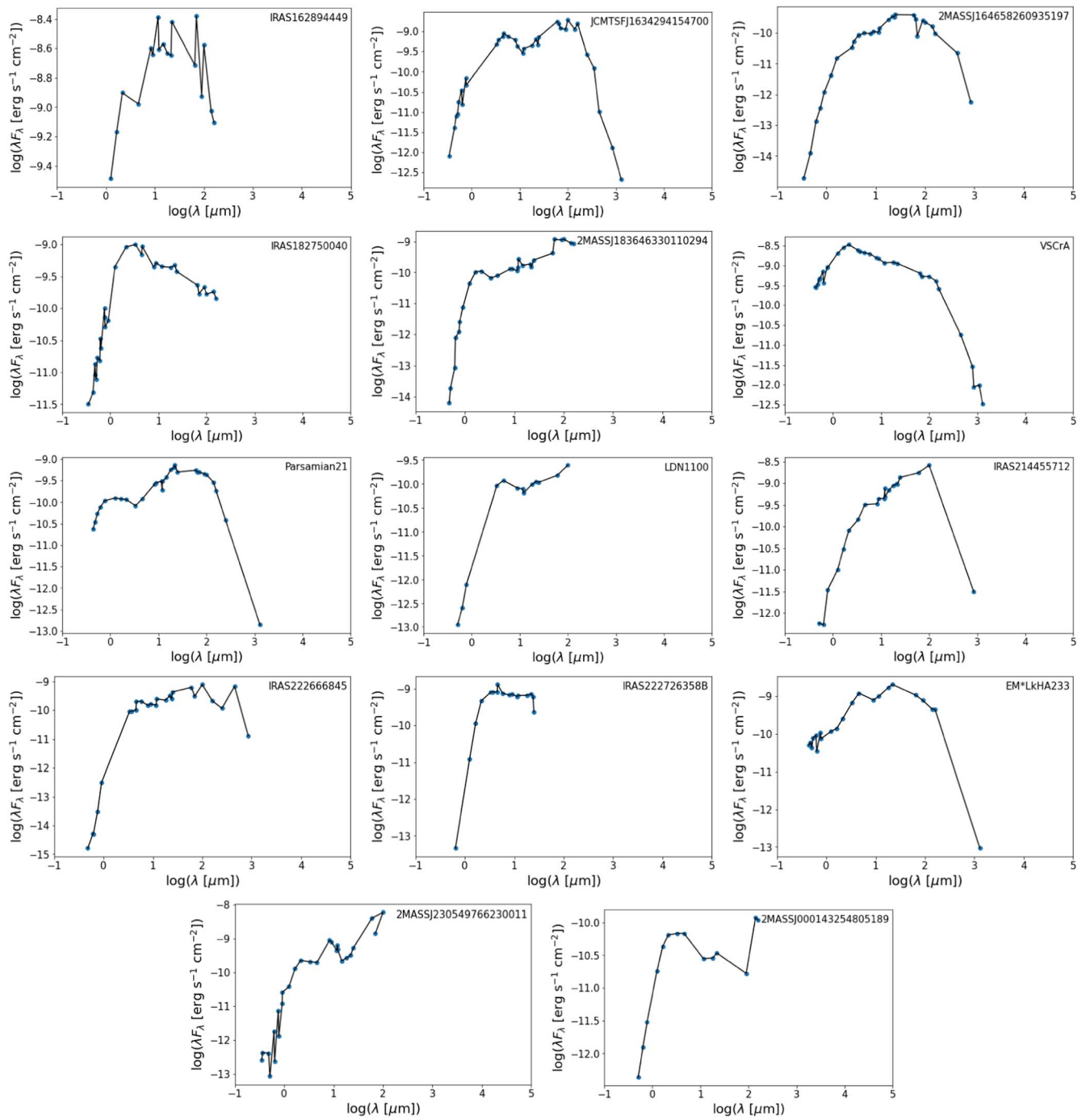


Figure 9. Spectral energy distributions of the YSOs.

Appendix D

In Table 8 we show the millimeter fluxes and the disk and dust masses computed in the literature for our Class I sample.


Table 8
Disk Masses for the Class I Targets from Gas Kinematics

ID	Name	Distance (pc)	F_{λ} (mJy)	λ (mm)	M_{dust} (M_{\oplus})	M_{disk} (M_{\oplus})	References
T1-01	CG2010 IRAS 032203035N	219.8 ± 16.2	78.9 ± 0.9	1.3	167.5 ± 24.8	0.0558 ± 0.0083	1
T1-02	2MASS J033312843121241	319.5 ± 23.7	42.4 ± 0.5	1.3	190.2 ± 28.3	0.0634 ± 0.0094	2
T1-05	BHS98 MHO1	134.0 ± 7.0	217.0 ± 0.8	1.3	171.0 ± 17.9	0.0570 ± 0.0060	3
T1-06	BHS98 MHO2	131.0 ± 2.9	133.0 ± 0.8	1.3	100.5 ± 4.5	0.0335 ± 0.0015	3
T1-07	IRAS 041692702	129.5 ± 12.9	200.0 ± 50.0	1.3	147.4 ± 47.1	0.0491 ± 0.0157	4
T1-08	MDM2001 CFHT BDTau19	155.9 ± 15.6	18.5 ± 0.90	0.9	7.2 ± 1.5	0.0024 ± 0.0005	5
T1-10	VFS Tau	133.9 ± 2.4	2.3 ± 0.14	1.3	1.8 ± 0.1	0.0006 ± 0.0000	6
T1-11	2MASS J042200692657324	133.9 ± 2.4	341.0 ± 34.10	0.9	97.3 ± 10.3	0.0324 ± 0.0034	7
T1-12*	VDG Tau	125.3 ± 1.9	42.71 ± 0.64	3.0	324.6 ± 11.0	0.1082 ± 0.0037	8
T1-14*	Haro 613	128.6 ± 1.6	25.0 ± 0.08	3.0	199.8 ± 5.0	0.0666 ± 0.0017	8
T1-15	IRAS 042952251	160.76 ± 16.1	110.0 ± 50.00	1.3	124.9 ± 62.0	0.0416 ± 0.0207	4
T1-17	IRAS 043812540	141.8 ± 1.4	27.9 ± 0.20	1.3	24.6 ± 5.0	0.0082 ± 0.0002	9
T1-22	Parenago 2649	398.5 ± 2.5	15.0 ± 3.00	1.3	104.7 ± 21.0	0.0349 ± 0.0070	10
T1-28	2MASS J054050590805487	440 ± 44	23.5 ± 0.72	0.9	72.4 ± 14.6	0.0241 ± 0.0049	11
T1-29	2MASS J054049910806084	440 ± 44	3.3 ± 0.56	0.9	10.2 ± 2.7	0.0034 ± 0.0009	11
T1-30	IRAS 054050117	420 ± 42	68.2 ± 1.56	0.9	191.5 ± 38.6	0.0638 ± 0.0129	11
T1-32	VV1818 Ori	633.4 ± 22.7	3.3 ± 0.07	1.3	58.2 ± 4.3	0.0194 ± 0.0014	12
T1-35*	WL 16	138.4 ± 2.6	4.4 ± 0.07	1.3	3.7 ± 0.2	0.0012 ± 0.0001	13
T1-37	IRAS 162894449	350.3 ± 2.5	27.0 ± 3.00	1.3	145.6 ± 16.3	0.0485 ± 0.0054	14
T1-42	VS CrA	160.5 ± 1.8	271.0 ± 0.80	1.3	306.7 ± 6.9	0.1022 ± 0.0023	15
T1-43	Parsamian 21	400 ± 100	33.9 ± 0.10	1.3	214.4 ± 107.2	0.0715 ± 0.0357	14
T2-09	03283968+3117321*	293 ± 22	5.16 ± 0.22	1.1	12.8 ± 0.8	0.0043 ± 0.0003	2
T2-10	J03285842+3122175*	293 ± 22	4.57 ± 0.16	1.1	11.3 ± 0.6	0.0038 ± 0.0002	2
T2-11	J03290149+3120208*	293 ± 22	3.10 ± 0.64	1.1	7.7 ± 2.2	0.0026 ± 0.0007	2
T2-12	SVS 13 (V512 Per)	293 ± 22	257.1 ± 2.9	1.3	969.7 ± 15.5	0.3232 ± 0.00512	1
T2-13	LAL96 213	293 ± 22	86.4 ± 0.2	1.3	318.5 ± 0.9	0.1063 ± 0.0003	2
T2-17	J03292003+3124076*	293 ± 22	1.0 ± 0.3	1.3	3.8 ± 1.6	0.0013 ± 0.0005	16
T2-01	IRS2	160	616.9 ± 1.0	1.3	693.8 ± 1.6	0.2313 ± 0.0005	15
T2-02	IRS5a	160	522.0 ± 1.3	1.3	587.1 ± 2.1	0.1957 ± 0.0007	15
T2-04	HH 100 IR	160	394.4 ± 1.5	1.3	443.5 ± 8.0	0.1478 ± 0.0027	15
T2-06	HH 26 IRS	450	145.4 ± 3.8	0.9	468.7 ± 18.1	0.1562 ± 0.0060	11
T2-07	HH 34 IRS	460	677.6 ± 14.2	0.9	2282.7 ± 67.7	0.7609 ± 0.0226	11
T2-08	HH 46 IRS	450	11.0 ± 0.01	3.0	1126.8 ± 14.5	0.3756 ± 0.0048	17
T3-01	B335	106 ± 15	28 ± 0.2	1.3	13.8 ± 3.9	0.0041 ± 0.0011	18
T3-02	IRAS 16253–2429	144 ± 9	10.1 ± 0.4	1.3	9.2 ± 1.2	0.0028 ± 0.0004	19
T3-03	VLA 1623A	144 ± 9	141.8 ± 5.9	1.3	129 ± 16	0.0388 ± 0.0049	20
T3-04	IRAS 15389–3559	155 ± 4	6.98 ± 0.12	1.2	5.9 ± 0.3	0.0018 ± 0.0001	21
T3-05	Lupus3–MMS	162 ± 3	185.1 ± 0.2	1.3	213 ± 8	0.0634 ± 0.0024	22
T3-06	L1455–IRS1	293 ± 22	46.5 ± 0.5	1.3	175 ± 26	0.0526 ± 0.0048	1
T3-07	IRAS 4A2	293 ± 22	434.2 ± 7.9	1.3	1637 ± 148	0.4916 ± 0.0444	1
T3-08	L1157	352 ± 19	181 ± 30	1.3	985 ± 195	0.2956 ± 0.0586	23
T3-09	HH 212	400 ± 40	186 ± 4	0.9	474 ± 95	0.1423 ± 0.0285	11
T3-10	L1527	141 ± 9	23 ± 0.11	3.0	241 ± 39	0.0723 ± 0.0117	24
T3-11	L1551–IRS5	141 ± 9	602.2 ± 55.9	1.3	526 ± 83	0.1580 ± 0.0025	25
T3-12	TMC1A	141 ± 9	240 ± 24	1.3	210 ± 34	0.0631 ± 0.0102	26
T3-13	L1489 IRS	141 ± 9	59 ± 5	1.3	52 ± 8	0.0155 ± 0.0023	27
T3-13	L1551–NE	141 ± 9	600 ± 1	0.9	187 ± 24	0.0562 ± 0.0072	28
T3-14	WL 12	144 ± 9	71.1 ± 0.4	1.3	62.1 ± 7.9	0.0187 ± 0.0024	15
T3-15	Elias 29	144 ± 9	17.2 ± 0.2	1.3	15.6 ± 2.0	0.0047 ± 0.0006	13
T3-16	IRS 63	144 ± 9	335. ± 18	1.3	305 ± 38	0.0916 ± 0.0114	29
T3-17	IRS 43	144 ± 9	16.9 ± 0.3	1.3	15.4 ± 1.9	0.0046 ± 0.0006	13
T3-18	RCrA IRS 7B	155 ± 4	372 ± 1	1.3	393 ± 17	0.1180 ± 0.0051	15
T3-19	HH 111	411 ± 41	285 ± 40	1.3	187 ± 24	0.0562 ± 0.0072	30

Table 8
(Continued)

ID	Name	Distance (pc)	F_{λ} (mJy)	λ (mm)	M_{dust} (M_{\oplus})	M_{disk} (M_{\oplus})	References
T3-20	EC 53	436 ± 9	139.7 ± 1.2	0.9	381 ± 16	0.1144 ± 0.0048	31

Note. References: 1—Tobin et al. (2018), 2—Tychoniec et al. (2020), 3—Akeson & Jensen (2014), 4—SMA; Sheehan & Eisner (2017), 5—ALMA: 2016.1.01511.S, 6—Akeson et al. (2019), 7—Villenave et al. (2020), 8—Harrison et al. (2019), 9—van ’t Hoff et al. (2020), 10—ALMA: 2019.1.01813.S, 11—Tobin et al. (2020), 12—Dutta et al. (2020), 13—Sadavoy et al. (2019), 14—Kóspál et al. (2021) 15—ALMA: 2019.1.01792.S, 16—Yang et al. (2021), 17—Zhang et al. (2016), 18—Bjerkeli et al. (2019), 19—Hsieh et al. (2019a), 20—Sadavoy et al. (2018), 21—Okoda et al. (2018), 22—Yen et al. (2017), 23—Chiang et al. (2012), 24—Nakatani et al. (2020), 25—circumbinary disk, flux averaged of natural and uniform weighting (Cruz-Sáenz de Miera et al. 2019), 26—Harsono et al. (2021), 27—Sai et al. (2020), 28—flux of circumbinary disk (Takakuwa et al. 2017), 29—Segura-Cox et al. (2020), 30—Lee (2010), 31—Lee et al. (2020).

ORCID iDsEleonora Fiorellino  <https://orcid.org/0000-0002-5261-6216>Łukasz Tychoniec  <https://orcid.org/0000-0002-9470-2358>Fernando Cruz-Sáenz de Miera  <https://orcid.org/0000-0002-4283-2185>Simone Antonucci  <https://orcid.org/0000-0002-0666-3847>Ágnes Kóspál  <https://orcid.org/0000-0001-7157-6275>Carlo F. Manara  <https://orcid.org/0000-0003-3562-262X>Brunella Nisini  <https://orcid.org/0000-0002-9190-0113>Giovanni Rosotti  <https://orcid.org/0000-0003-4853-5736>**References**

- Abazajian, K. N., Adelman-McCarthy, J. K., Agüeros, M. A., et al. 2009, *ApJS*, **182**, 543
- Ahn, C. P., Alexandroff, R., Allende Prieto, C., et al. 2012, *ApJS*, **203**, 21
- Akeson, R. L., & Jensen, E. L. N. 2014, *ApJ*, **784**, 62
- Akeson, R. L., Jensen, E. L. N., Carpenter, J., et al. 2019, *ApJ*, **872**, 158
- Alam, S., Albareti, F. D., Prieto, C. A., et al. 2015, *ApJS*, **219**, 12
- Alcalá, J. M., Natta, A., Manara, C. F., et al. 2014, *A&A*, **561**, A2
- Alcalá, J. M., Manara, C. F., Natta, A., et al. 2017, *A&A*, **600**, A20
- Alves, F. O., Caselli, P., Girart, J. M., et al. 2019, *Sci*, **366**, 90
- Andrews, S. M., Rosenfeld, K. A., Kraus, A. L., & Wilner, D. J. 2013, *ApJ*, **771**, 129
- Andrews, S. M., & Williams, J. P. 2007, *ApJ*, **671**, 1800
- Anglada, G., & Rodríguez, L. F. 2002, *RMxAA*, **38**, 13
- Ansdell, M., Williams, J. P., Manara, C. F., et al. 2017, *AJ*, **153**, 240
- Ansdell, M., Williams, J. P., van der Marel, N., et al. 2016, *ApJ*, **828**, 46
- Antonucci, S., Nisini, B., Giannini, T., & Lorenzetti, D. 2008, *A&A*, **479**, 503
- Aso, Y., Ohashi, N., Saigo, K., et al. 2015, *ApJ*, **812**, 27
- Bailer-Jones, C. A. L., Farnocchia, D., Ye, Q., Meech, K. J., & Micheli, M. 2020, *A&A*, **634**, A14
- Beichman, C. A., Neugebauer, G., Habing, H. J., Clegg, P. E., & Chester, T. J. 1988, *Infrared Astronomical Satellite (IRAS) Catalogs and Atlases. Volume 1: Explanatory Supplement*
- Bianchi, L., Herald, J., Efremova, B., et al. 2011, *Ap&SS*, **335**, 161
- Bjerkeli, P., Ramsey, J. P., Harsono, D., et al. 2019, *A&A*, **631**, A64
- Brinch, C., & Jørgensen, J. K. 2013, *A&A*, **559**, A82
- Calvet, N., & Gullbring, E. 1998, *ApJ*, **509**, 802
- Calvet, N., Muzerolle, J., Briceño, C., et al. 2004, *AJ*, **128**, 1294
- Chiang, H.-F., Looney, L. W., & Tobin, J. J. 2012, *ApJ*, **756**, 168
- Choi, M., Tatematsu, K., & Kang, M. 2010, *ApJL*, **723**, L34
- Chou, T.-L., Takakuwa, S., Yen, H.-W., Ohashi, N., & Ho, P. T. P. 2014, *ApJ*, **796**, 70
- Codella, C., Cabrit, S., Gueth, F., et al. 2014, *A&A*, **568**, L5
- Connelley, M. S., & Greene, T. P. 2010, *AJ*, **140**, 1214
- Connelley, M. S., Reipurth, B., & Tokunaga, A. T. 2007, *AJ*, **133**, 1528
- Connelley, M. S., Reipurth, B., & Tokunaga, A. T. 2008, *AJ*, **135**, 2496
- Cruz-Sáenz de Miera, F., Kóspál, Á., Abraham, P., Liu, H. B., & Takami, M. 2019, *ApJL*, **882**, L4
- Cutri, R. M., Skrutskie, M. F., van Dyk, S., et al. 2003, *yCat*, **2246**, 0
- Cutri, R. M., Wright, E. L., Conrow, T., et al. 2012, *Explanatory Supplement to the WISE All-Sky Data Release Products*, <http://wise2.ipac.caltech.edu/docs/release/allsky/expsup/index.html>
- Davies, C. L. 2021, *SoftX*, **14**, 100687
- Di Francesco, J., Johnstone, D., Kirk, H., MacKenzie, T., & Ledwosinska, E. 2008, *ApJS*, **175**, 277
- Doppmann, G. W., Greene, T. P., Covey, K. R., & Lada, C. J. 2005, *AJ*, **130**, 1145
- Dunham, M. M., Allen, L. E., Evans, N. J., I, et al. 2015, *ApJS*, **220**, 11
- Dunham, M. M., Arce, H. G., Allen, L. E., et al. 2013, *AJ*, **145**, 94
- Dunham, M. M., Crapsi, A., Evans, N. J., I, et al. 2008, *ApJS*, **179**, 249
- Dunham, M. M., Stutz, A. M., Allen, L. E., et al. 2014, in *Protostars and Planets VI*, ed. H. Beuther et al. (Tucson, AZ: Univ Arizona Press), 195
- Dutta, S., Lee, C.-F., Liu, T., et al. 2020, *ApJS*, **251**, 20
- Dzib, S. A., Loinard, L., Ortiz-León, G. N., Rodríguez, L. F., & Galli, P. A. B. 2018, *ApJ*, **867**, 151
- Eisloffel, J., Guenther, E., Hessman, F. V., et al. 1991, *ApJL*, **383**, L19
- Enoch, M. L., Evans, N. J., I, Sargent, A. I., & Glenn, J. 2009, *ApJ*, **692**, 973
- Evans, N. J., I, Allen, L. E., Blake, G. A., et al. 2003, *PASP*, **115**, 965
- European Space Agency 2017a, *Herschel PACS Point Source Catalogue, v1.0*, doi:10.5270/esa-rw7rbo7
- European Space Agency 2017b, *Herschel SPIRE Point Source Catalogue, v1.0*, doi:10.5270/esa-6gfkpzh
- Fairlamb, J. R., Oudmaijer, R. D., Mendigutía, I., Ilee, J. D., & van den Ancker, M. E. 2015, *MNRAS*, **453**, 976
- Fiorellino, E., Manara, C. F., Nisini, B., et al. 2021, *A&A*, **650**, A43
- Fiorellino, E., Tychoniec, L., Manara, C. F., et al. 2022, *ApJL*, **937**, L9
- Fischer, W., Edwards, S., Hillenbrand, L., & Kwan, J. 2011, *ApJ*, **730**, 73
- Fischer, W. J., Hillenbrand, L. A., Herczeg, G. J., et al. 2022, arXiv:2203.11257
- Froebrich, D. 2005, *ApJS*, **156**, 169
- Furlan, E., McClure, M., Calvet, N., et al. 2008, *ApJS*, **176**, 184
- Furlan, E., Fischer, W. J., Ali, B., et al. 2016, *ApJS*, **224**, 5
- Gaia Collaboration 2018, *yCat*, **1345**, 0
- Gaia Collaboration, Brown, A. G. A., Vallenari, A., et al. 2021, *A&A*, **649**, A1
- Galli, P. A. B., Bouy, H., Olivares, J., et al. 2020, *A&A*, **634**, A98
- Girart, J. M., Rodríguez, L. F., & Curiel, S. 2000, *ApJL*, **544**, L153
- Green, J. D., Evans, N. J., II, Jørgensen, J. K., et al. 2013, *ApJ*, **770**, 123
- Greene, T. P., Wilking, B. A., Andre, P., Young, E. T., & Lada, C. J. 1994, *ApJ*, **434**, 614
- Guieu, S., Dougados, C., Monin, J.-L., Magnier, E., & Martín, E. L. 2006, *A&A*, **446**, 485
- Gullbring, E., Hartmann, L., Briceño, C., & Calvet, N. 1998, *ApJ*, **492**, 323
- Harrison, R. E., Looney, L. W., Stephens, I. W., et al. 2019, *ApJL*, **877**, L2
- Harsono, D., van der Wiel, M. H. D., Bjerkeli, P., et al. 2021, *A&A*, **646**, A72
- Hartmann, L., Calvet, N., Gullbring, E., & D’Alessio, P. 1998, *ApJ*, **495**, 385
- Hartmann, L., Herczeg, G., & Calvet, N. 2016, *ARA&A*, **54**, 135
- Henden, A. A., Levine, S., Terrell, D., & Welch, D. L. 2015, *AAS Meeting*, **225**, 336.16
- Hennebelle, P., Commerçon, B., Lee, Y.-N., & Charnoz, S. 2020, *A&A*, **635**, A67
- Herczeg, G. J., & Hillenbrand, L. A. 2008, *ApJ*, **681**, 594
- Hillenbrand, L. A., Strom, S. E., Vrba, F. J., & Keene, J. 1992, *ApJ*, **397**, 613
- Hilton, J., & Lahulla, J. F. 1995, *A&AS*, **113**, 325
- Howard, C. D., Sandell, G., Vacca, W. D., et al. 2013, *ApJ*, **776**, 21
- Hsieh, T.-H., Hirano, N., Belloche, A., et al. 2019a, *ApJ*, **871**, 100
- Hsieh, T.-H., Murillo, N. M., Belloche, A., et al. 2019b, *ApJ*, **884**, 149
- Ingleby, L., Calvet, N., Herczeg, G., et al. 2013, *ApJ*, **767**, 112
- Ishihara, D., Onaka, T., Kataza, H., et al. 2010, *A&A*, **514**, A1
- Karska, A., Kaufman, M. J., Kristensen, L. E., et al. 2018, *ApJS*, **235**, 30
- Kóspál, Á., Abraham, P., Apai, D., et al. 2008, *MNRAS*, **383**, 1015
- Kóspál, Á., Cruz-Sáenz de Miera, F., White, J. A., et al. 2021, *ApJS*, **256**, 30

- Kratter, K., & Lodato, G. 2016, *ARA&A*, 54, 271
- Krolkowsky, D. M., Kraus, A. L., & Rizzuto, A. C. 2021, *AJ*, 162, 110
- Kwon, W., Fernandez-Lopez, M., Stephens, I. W., & Looney, L. W. 2015, *ApJ*, 814, 43
- Lada, C. J. 1991, in *The Physics of Star Formation and Early Stellar Evolution*, NATO Advanced Study Institute (ASI) Series C, Vol. 342, ed. C. J. Lada & N. D. Kylafis (Dordrecht: Kluwer), 329
- Laos, S., Greene, T. P., Najita, J. R., & Stassun, K. G. 2021, *ApJ*, 921, 110
- Lee, C.-F. 2010, *ApJ*, 725, 712
- Lee, S., Lee, J.-E., Aikawa, Y., Herczeg, G., & Johnstone, D. 2020, *ApJ*, 889, 20
- Lindberg, J. E., Jørgensen, J. K., Brinch, C., et al. 2014, *A&A*, 566, A74
- Lodato, G., Scardoni, C. E., Manara, C. F., & Testi, L. 2017, *MNRAS*, 472, 4700
- Lommen, D., Jørgensen, J. K., van Dishoeck, E. F., & Crapsi, A. 2008, *A&A*, 481, 141
- Looney, L. W., Mundy, L. G., & Welch, W. J. 1997, *ApJL*, 484, L157
- Lorenzetti, D., Antonucci, S., Giannini, T., et al. 2013, *Ap&SS*, 343, 535
- Manara, C. F., Ansdell, M., Rosotti, G. P., et al. 2022, arXiv:2203.09930
- Manara, C. F., Fedele, D., Herczeg, G. J., & Teixeira, P. S. 2016, *A&A*, 585, A136
- Mannings, V., & Emerson, J. P. 1994, *MNRAS*, 267, 361
- Marsh, K. A., Kirk, J. M., Andre, P., et al. 2016, *MNRAS*, 459, 342
- Miotello, A., Kamp, I., Birnstiel, T., Cleves, L. I., & Kataoka, A. 2022, arXiv:2203.09818
- Miotello, A., Testi, L., Lodato, G., et al. 2014, *A&A*, 567, A32
- Murillo, N. M., & Lai, S. -P. 2013, *ApJL*, 764, L15
- Muzerolle, J., Hartmann, L., & Calvet, N. 1998, *AJ*, 116, 2965
- Nakatani, R., Liu, H. B., Ohashi, S., et al. 2020, *ApJL*, 895, L2
- Nisini, B., Antonucci, S., Giannini, T., & Lorenzetti, D. 2005, *A&A*, 429, 543
- Okoda, Y., Oya, Y., Sakai, N., et al. 2018, *ApJL*, 864, L25
- Olofsson, S., & Olofsson, G. 2009, *A&A*, 498, 455
- Ortiz-León, G. N., Dzib, S. A., Kounkel, M. A., et al. 2017, *ApJ*, 834, 143
- Ortiz-León, G. N., Loinard, L., Dzib, S. A., et al. 2018, *ApJ*, 865, 73
- Ossenkopf, V., & Henning, T. 1994, *A&A*, 291, 943
- Page, M. J., Brindle, C., Talavera, A., et al. 2012, *MNRAS*, 426, 903
- Palla, F., & Stahler, S. W. 1990, *ApJL*, 360, L47
- Palla, F., & Stahler, S. W. 1993, *ApJ*, 418, 414
- Pascucci, I., Testi, L., Herczeg, G. J., et al. 2016, *ApJ*, 831, 125
- Pecaut, M. J., & Mamajek, E. E. 2013, *ApJS*, 208, 9
- Pezzuto, S., Benedettini, M., Di Francesco, J., et al. 2021, *A&A*, 645, A55
- Prato, L., Lockhart, K. E., Johns-Krull, C. M., & Rayner, J. T. 2009, *AJ*, 137, 3931
- Purser, S. J. D., Ainsworth, R. E., Ray, T. P., et al. 2018, *MNRAS*, 481, 5532
- Reipurth, B., Rodríguez, L. F., Anglada, G., & Bally, J. 2002, *ApJ*, 124, 1045
- Reipurth, B., Yu, K. C., Rodríguez, L. F., Heathcote, S., & Bally, J. 1999, *A&A*, 352, L83
- Ribas, Á., Espaillat, C. C., Macías, E., et al. 2017, *ApJ*, 849, 63
- Rigliaco, E., Natta, A., Testi, L., et al. 2012, *A&A*, 548, A56
- Rosotti, G. P., Clarke, C. J., Manara, C. F., & Facchini, S. 2017, *MNRAS*, 468, 1631
- Rugel, M., Fedele, D., & Herczeg, G. 2018, *A&A*, 609, A70
- Sadavoy, S. I., Myers, P. C., Stephens, I. W., et al. 2018, *ApJ*, 859, 165
- Sadavoy, S. I., Stephens, I. W., Myers, P. C., et al. 2019, *ApJS*, 245, 2
- Sai, J., Ohashi, N., Saigo, K., et al. 2020, *ApJ*, 893, 51
- Schneider, P. C., Günther, H. M., & France, K. 2020, *Galax*, 8, 27
- Segura-Cox, D. M., Schmiedeke, A., Pineda, J. E., et al. 2020, *Natur*, 586, 228
- Sheehan, P. D., & Eisner, J. A. 2017, *ApJ*, 851, 45
- Sheehan, P. D., & Eisner, J. A. 2018, *ApJ*, 857, 18
- Sheehan, P. D., Tobin, J. J., Looney, L. W., & Megeath, S. T. 2022, *ApJ*, 929, 76
- Shimajiri, Y., Kitamura, Y., Nakamura, F., et al. 2015, *ApJS*, 217, 7
- Siess, L., Dufour, E., & Forestini, M. 2000, *A&A*, 358, 593
- Tabone, B., Rosotti, G. P., Cridland, A. J., Armitage, P. J., & Lodato, G. 2022, *MNRAS*, 512, 2290
- Takakuwa, S., Saigo, K., Matsumoto, T., et al. 2017, *ApJ*, 837, 86
- Takakuwa, S., Saito, M., Lim, J., & Saigo, K. 2013, *ApJ*, 776, 51
- Testi, L., Natta, A., Manara, C. F., et al. 2022, *A&A*, 663, A98
- Tobin, J. J., Cox, E. G., & Looney, L. W. 2022, *ApJ*, 928, 61
- Tobin, J. J., Hartmann, L., Chiang, H. -F., et al. 2012, *Natur*, 492, 83
- Tobin, J. J., Kratter, K. M., Persson, M. V., et al. 2016b, *Natur*, 538, 483
- Tobin, J. J., Looney, L. W., Li, Z. -Y., et al. 2016a, *ApJ*, 818, 73
- Tobin, J. J., Looney, L. W., Li, Z. -Y., et al. 2018, *ApJ*, 867, 43
- Tobin, J. J., Sheehan, P. D., Megeath, S. T., et al. 2020, *ApJ*, 890, 130
- Tychoniec, L., Manara, C. F., Rosotti, G. P., et al. 2020, *A&A*, 640, A19
- van't Hoff, M. L. R., Harsono, D., Tobin, J. J., et al. 2020, *ApJ*, 901, 166
- Villenave, M., Ménard, F., Dent, W. R. F., et al. 2020, *A&A*, 642, A164
- Vorobyov, E. I., Elbakyan, V. G., Liu, H. B., & Takami, M. 2021, *A&A*, 647, A44
- White, R. J., & Hillenbrand, L. A. 2004, *ApJ*, 616, 998
- Wouterloot, J. G. A., & Brand, J. 1989, *A&AS*, 80, 149
- Yamamura, I., Makiuti, S., Ikeda, N., et al. 2010, *yCat*, 2298, 0
- Yan, Q.-Z., Zhang, B., Xu, Y., et al. 2019, *A&A*, 624, A6
- Yang, Y.-L., Green, J. D., Evans, N. J., II, et al. 2018, *ApJ*, 860, 174
- Yang, Y.-L., Sakai, N., Zhang, Y., et al. 2021, *ApJ*, 910, 20
- Yen, H.-W., Koch, P. M., Takakuwa, S., et al. 2017, *ApJ*, 834, 178
- Yen, H.-W., Takakuwa, S., Koch, P. M., et al. 2015, *ApJ*, 812, 129
- Zari, E., Hashemi, H., Brown, A. G. A., Jardine, K., & de Zeeuw, P. T. 2018, *A&A*, 620, A172
- Zhang, Y., Arce, H. G., Mardones, D., et al. 2016, *ApJ*, 832, 158
- Zhu, Z., Zhang, S., Jiang, Y. -F., et al. 2019, *ApJL*, 877, L18
- Zucker, C., Speagle, J. S., Schlafly, E. F., et al. 2019, *ApJ*, 879, 125